2012-03-14

Estimated Instability and Breaking of Internal Waves due to Time-dependent Shear

Leonardo A. Latorre
Brigham Young University - Provo

Estimated Instability and Breaking of Internal Waves due to Time-dependent Shear

Leonardo A. Latorre

A thesis submitted to the faculty of
Brigham Young University
in partial fulfillment of the requirements for the degree of

Master of Science

Julie C. Vanderhoff, Chair
Steven E. Gorrell
Tadd T. Truscott

Department of Mechanical Engineering

Brigham Young University

April 2012

ABSTRACT

Estimated Instability and Breaking of Internal Waves
due to Time-dependent Shear

Leonardo A. Latorre
Department of Mechanical Engineering, BYU
Master of Science

The effects of propagation of a short internal gravity wave through an inertia wave on internal wave stability is analyzed and parameterized. The interactions are specifically between a short wave packet and a large inertia wave packet. The short wave packet is a wave bounded with a Gaussian envelope with high frequencies and scales in the hundreds of meters horizontally and tens of meters vertically. The inertia wave packet is also an enveloped wave but with frequencies close to the rotation of the earth and scales in the thousands of meters in the horizontal and hundreds of meters in the vertical. The wave-wave interactions are modeled using ray theory and 2d non-linear numerical models. Ray tracing is used because it is less computationally expensive, however it fails at regions of strong refraction also known as caustics. To measure stability the steepness is calculated from the 2d non-linear methods and it is compared with estimates found in the linear theory. It is determined that the estimates of the short wave steepness from linear theory are qualitatively comparable. A quantifiable comparison, although more difficult, resulted in adjustment factors to the ray tracing results. It is also found that for the particular cases modeled, convective instabilities are predominant and the influence of the shear exerted by the large inertia wave is insignificant. Instability timescales are included in the stability analysis and estimates of overturning and wave-breaking are developed for different wave-wave interactions. From the stability analysis it is found that in general the faster the short wave propagates the more likely it is to conform to both of the conditions required for wave breaking (i.e presence of instabilities and instability timescales longer than the timescale of the short wave).

Keywords: Internal gravity waves instability, oceanic energy dissipation, stratified fluids, Leonardo Latorre, Julie Vanderhoff

ACKNOWLEDGMENTS

I would never have been able to finish my dissertation without the guidance of my committee members, help from friends, and support from my family and wife.

I would like express my deepest gratitude to my advisor, Dr. Julie Vanderhoff, for all the time and dedication that she has invested in me. I am grateful for her guidance and the knowledge that she shared with me for the past two years. She has facilitated an excellent atmosphere for me to accomplish my research. I also would like to thank her for patiently correct my writing and for financially supporting my research.

I would also like to thank Dr. Gorrell and Dr. Truscott for their input and for their willingness to sacrifice some of their time and be part of my committee. Special thanks to Dr. Truscott, who was willing to join my committee half way through the research.

Many thanks also to the funding and support from the National Science Foundation grant CBET 0854131 and the NASA Rocky mountain consortium. Without their monetary contributions, our resources would have been very limited.

I also want to thank my colleagues Matthew, Ryan, Sean and Tyler at the fluid dynamics lab, who as good friends, were willing to help and give their best suggestions. Many thanks to Benjamin Hillyard, who became a close friend. I appreciated his humor and company during my time here at Brigham Young University.

Finally, I want to thank my wife, Kami Latorre. She has always been very supportive in all of my pursuits. She was always there inspiring confidence and keeping me motivated through the good times and bad. She was always willing to undertake most of the responsibilities of the home in order for me to work on my research. She was also ready and eager to help me correct my writing and always improved my compositions.

TABLE OF CONTENTS

LIST OF TABLES

LIST OF FIGURES

CHAPTER 1. INTRODUCTION

1.1 Motivation

Vertical mixing is a dominant factor of global oceanic energy equilibrium. The breaking of internal gravity waves produces significant fluxes of momentum and heat making it an important contributor to oceanic turbulence and vertical mixing. Hence, it is of general interest to quantify the energy related to internal gravity wave propagation and breaking as a potential source of renewable energy and to understand the global effects of energy dissipation due to internal waves breaking.

Internal gravity waves are common in the ocean and the atmosphere because of their stably-stratified characteristics. A stably-stratified medium is one characterized by a density distribution that increases with decreasing elevation. The generation of waves occurs when disturbances to the density field are introduced and the perturbation occurs at a frequency lower than the buoyancy frequency (natural frequency) of the medium. This buoyancy frequency depends on the stratification of the medium $N = f(d\rho/dz)$. When particles are displaced from their neutrally buoyant position as seen in figure 1.1, buoyancy forces will work to restore the particles to their initial location. Inertial forces drive the particle past its neutral location and once again buoyancy forces act to restore the particle back to the neutral state. This cyclic process continues and consequently generates internal gravity waves. Internal gravity waves, unlike surface waves, are not confined to a fluid interface. These waves propagate in the vertical and horizontal planes (i.e. three dimensions). Thus, internal waves have wavelengths and corresponding wave-numbers in all three dimensions. The perturbations to the density field which cause internal waves occur in diverse forms since virtually any disturbance can generate internal waves. Some common forms of internal wave generation are air or water currents moving over topography, vortices, windshear at the ocean surface or the breakdown of internal waves.

Although internal waves exist in the atmosphere and oceans, in this study the attention is on oceanic waves. Ocean waves range in magnitude from inertia waves induced by the frequency of

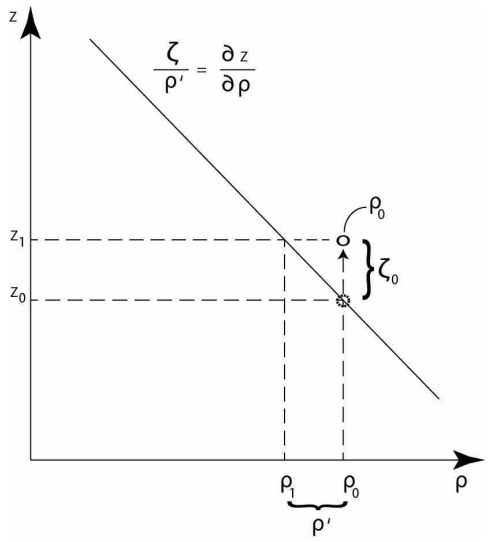

Figure 1.1: This is a representation of a density gradient for a stratified fluid. A force balance is performed on the particle that has been displaced from its neutral position to derive the buoyancy frequency of the medium

the rotation of the earth to short waves generated by the types of mechanisms mentioned previously. Large inertia waves have typical vertical wavelengths of hundreds of meters, limited by the depth of the ocean floor, and horizontal wavelengths of thousands of meters, limited by ocean basin scales. Short waves have vertical wavelengths of tens to hundreds of meters and horizontal wavelength scales of hundreds of meters.

Internal waves, in the same manner as surface waves, have significant energy and momentum associated with their propagation. The energy of internal waves propagates with the group velocity, perpendicular to the phases of the wave as seen in figure 1.2. When waves interact with other fluid phenomena their energy may be exchanged or dissipated. If this energy dissipation is in the form of wave breaking it results in turbulence. The turbulence induces vertical mixing which is an essential mechanism in the oceans which transports organisms, pollutants, nutrients and heat to deep ocean (Garrett [4]). In fact, diapycnal mixing (mixing across lines of constant density) in the ocean interior is primarily driven by internal wave breaking. Egbert and Ray [5] show with satellite altimeter data that approximately one Terawatt of tidal energy dissipation occurs in the open ocean through the scattering of surface tides into internal waves by ocean-bottom topography. Munk and Wunsch [6] also agree on the significant influence of internal wave breaking in the oceanic en-

ergy balance. The authors conclude that turbulence resulting from internal wave breaking provides potential energy that drives the global ocean circulation.

Current global scale models employed to describe energy budgets in the oceans lack the necessary resolution to define the influence of internal wave interactions and their related energy dissipation. Large scale models have inadequate resolution because turbulent mixing is typically represented by a diffusivity that is constant everywhere except right below the surface mixed layer. However, it has been shown that mixing in the real ocean is non-uniform in space and time, which in turn has profound implications in the ocean circulation (Simmons et al. [7]).

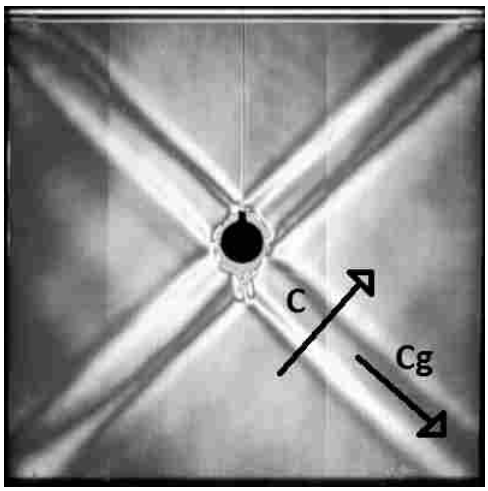

Figure 1.2: Internal waves generated by cylinder oscillating. The phases C and group velocity c_g are labeled and signaled by the arrows moving perpendicular to each other. The energy for internal waves moves with c_g perpendicular to the phases of the wave. In this picture, the dark and light rays propagating diagonally are the troughs and crests of the internal waves. Taken from `http://www.gfd-dennou.org/library/gfd$_$exp/exp$_$e/exp/iw/1/res.htm`.

- The first objective is to use a 2d fully non-linear model to compare and improve the linear model's amplitude approximations at regions of strong refraction where non-linearities exist. The improved amplitude approximations will be used in a stability analysis to define some of the short wave instabilities.

- The second objective is to perform a stability analysis and use short wave steepness and inertia wave shear to define convective and shear instabilities, which will be explained in the next chapter.

- The third objective is to use the linear model to simulate a spectrum of short internal waves interacting with an inertia wave and develop a map that demonstrates estimates of wave breaking as a function of initial wave properties such as steepness (vertical displacement with respect to depth) and wave group speed.

1.2 Literature review

The study and observation of internal gravity waves is difficult due to their non-linear nature, their range of scales, and because they coexist with many other phenomena in the oceans. An efficient alternative to observations is to simulate internal waves using linear and non-linear models, which has been common practice among researchers for the past 20 years. Numerical models are more accessible if the physics of the waves can be simplified, otherwise the models would be computationally prohibitive. These simplifications, though, result in limitations to both linear and non-linear models. Linear model assumptions break down with the presence of instabilities, which are inherently non-linear. Non-linear two-dimensional models lose validity when the waves break and the onset of turbulence appears. Whereas non-linear three-dimensional models will resolve initial wave breaking and some aspects of turbulence but at a much higher computational expense, depending on the resolution.

This research studies the interaction among internal waves and the resulting effects of these interactions on waves overturning and breaking. Linear and 2d non-linear models are used to simulate and analyze the connection between internal wave group speed, steepness (vertical displacement with respect to depth) and wave stability. In this literature review, common types of wave interactions are introduced, followed by previous work of other researchers on wave stability and breaking.

1.2.1 Internal gravity wave interactions

Early studies of internal gravity waves directed attention to the simpler case when internal gravity waves interact with a time-independent shear. During this type of interaction the vertical speed of the wave goes to zero as it propagates into an increasing velocity. Simultaneously, the horizontal component of the wave speed matches the ambient flow speed, thus the motion of the

wave is no longer upwards but only forward in the direction of the flow. This is defined as a critical level and a diagram of this type of interaction is presented in figure 1.3. These interactions are interesting because the momentum of the internal wave is transferred to the time-independent shear. Bretherton [8] used ray theory to examine interactions of packets of internal gravity waves

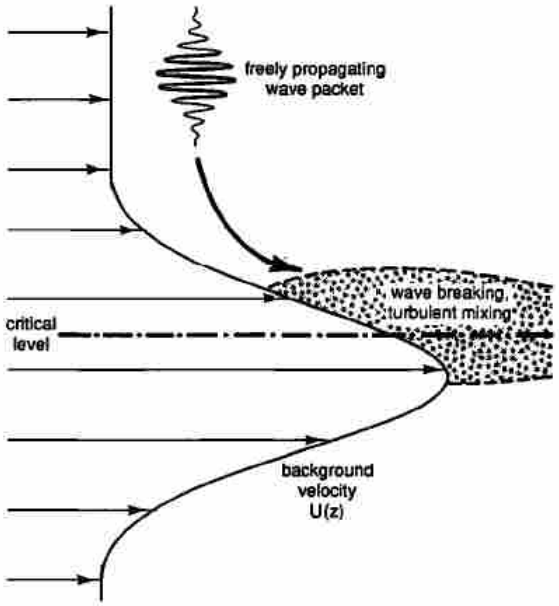

Figure 1.3: Interaction between an internal wave packet and a steady shear, which results in the energy of the wave being absorbed by the steady shear at an absorbing layer called critical level. Taken from Winters and D'Asaro [1]

in a shear flow. He concluded that a critical level may act as an effective energy absorbing layer to the waves preventing further vertical propagation of the waves. Winters and D'Asaro [1] used a 2d non-linear model to analyze these interactions and found that, for moderate wave amplitudes, the interaction portrays a critical level beyond which internal waves do not propagate. In the case of higher amplitude waves, the inertia waves overturn and break when encountering the steady shear. The topic of waves developing statically unstable conditions leading to breaking will be covered in more detail in the following subsection of the literature review.

A more complex interaction is that of an internal gravity wave with a time-dependent shear in the form of an inertia wave. In this case the short internal wave exhibits cyclical changes in the frequency and vertical wavenumber as it refracts throughout the interaction. No critical levels

are present during the encounter with inertia waves due to the time dependence of the interaction. Instead the short wave undergoes strong refractions that can alter the energy of the internal wave after it interacts. Broutman and Young [9] and Vanderhoff, Nomura, Rottman and Macaskill [10], using ray theory, demonstrated that wave packets are not absorbed but instead propagate through and may leave the inertia wave with permanent energy changes. These energy changes were denoted by significant variation in the short wave frequency and vertical group speed. Bruhwiler and Kaper [11] examined this scattering of the small scale internal waves. Their study was based on the ray tracing prototype developed by Broutman and Young [9]. In their analysis, Bruhwiler and Kaper, found a dramatic transport of wave energy from lower (inertia waves) to higher frequency (small scale) waves. Vanderhoff, Rottman and Broutman [12] found that a spectrum of incident narrow-banded short-waves approaching a short inertia wave packet, results in the spectrum broadening more quickly and more fully than when refracted by a large inertia wave packet. Therefore the time dependence of the shear has a significant effect on the dynamics of the interaction, since the momentum flux is generally from the time-dependent shear to the internal wave. Vanderhoff, et al. [10] expanded on the effects of time-dependence on wave-wave interactions using ray theory and non-linear models. They concluded that in order to understand and model correctly the role of Doppler spreading in realistic oceanic and atmospheric waves, critical levels observed in time-independent shears should not be assumed for inertia waves because the behavior of the waves is drastically different. Thus, making the result of the interaction considerably different between a steady shear and an inertia wave. In some cases when the short waves encounter the inertia wave with large initial amplitudes, they may overturn and break. Sartelet [13] utilized linear and non-linear models to simulate internal gravity wave packets with different frequencies, wavenumbers and amplitudes approaching a localized inertia wave. From this study Sartelet concluded that the effects of time-dependence of the inertia wave on wave breaking is only perceived when the wave packets have large initial amplitudes.

1.2.2 Stability and breaking of internal gravity waves

Internal gravity waves may propagate for long distances, but eventually if not absorbed they will grow or interact and overturn and break. The breaking of many internal waves significantly contributes to the overall energy balance in the oceans mixing and nutrient distribution as

mentioned in the introduction. These waves contain significant amounts of energy, which is evident due to their large scales ranging from tens of meters to hundreds of meters in the vertical direction and thousands of meters in the horizontal direction. Thus, it is crucial to comprehend the mechanisms leading to wave breaking, namely instabilities, in order to understand the significance of energy dissipation from internal waves.

Internal wave instabilities primarily exist in two forms: convective instabilities and shear instabilities. Convective instabilities occur when lines of constant density (isopycnals) become vertical generating an inverse density gradient, with heavier fluid over lighter. Figure 1.4 shows an overturning and breaking process driven by convective instabilities. Shear instabilities cause disturbances to the internal wave amplitude and wavenumber forcing the short wave to steepen because of the velocity gradient, resulting in wave overturning. Figure 1.5 shows a shear (Kelvin Helmholtz) instability between two fluids. A similar instability mechanism affects the short waves when they interact with the inertia wave. Typical parameters used to analyze these instabilities are the steepness of the waves and the Richardson number. Steepness is a measurement of the internal wave vertical displacement with respect to depth, which if greater than one indicates overturning. The Richardson number is a non-dimensional parameter that accounts for the influence of shear forces with respect to the strength of the stratification. When the Richardson number is less than 1/4 the wave is unstable. Thorpe [14] utilized analytical and numerical techniques to simulate inertia waves propagating in a thin, high density-gradient layer. As the inertia waves propagated through the thin layer, shear instabilities were formed in the same manner as when two layers with different velocities interact. Thorpe found that the minimum Richardson number for both the x-direction flow and the y-direction flow may be less than 1/4, provided that the ratio σ/f is sufficiently close to unity, where σ is the wave frequency and f is the Coriolis frequency-frequency of the rotation of the earth. This was a significant conclusion since the critical value of the Richardson number is defined as 1/4. Nonetheless, for waves with higher frequencies than the Coriolis frequency, the stability condition of the Richardson number being less than 1/4 still applies.

Interactions between an internal wave and a steady shear may result in the internal wave being absorbed (critical level discussed in previous section). However, instabilities may develop before the wave transfers its energy to the mean flow. In this case, steepness and the Richardson number can be used to parameterize instability. Winters and D'Asaro [1] performed simulations

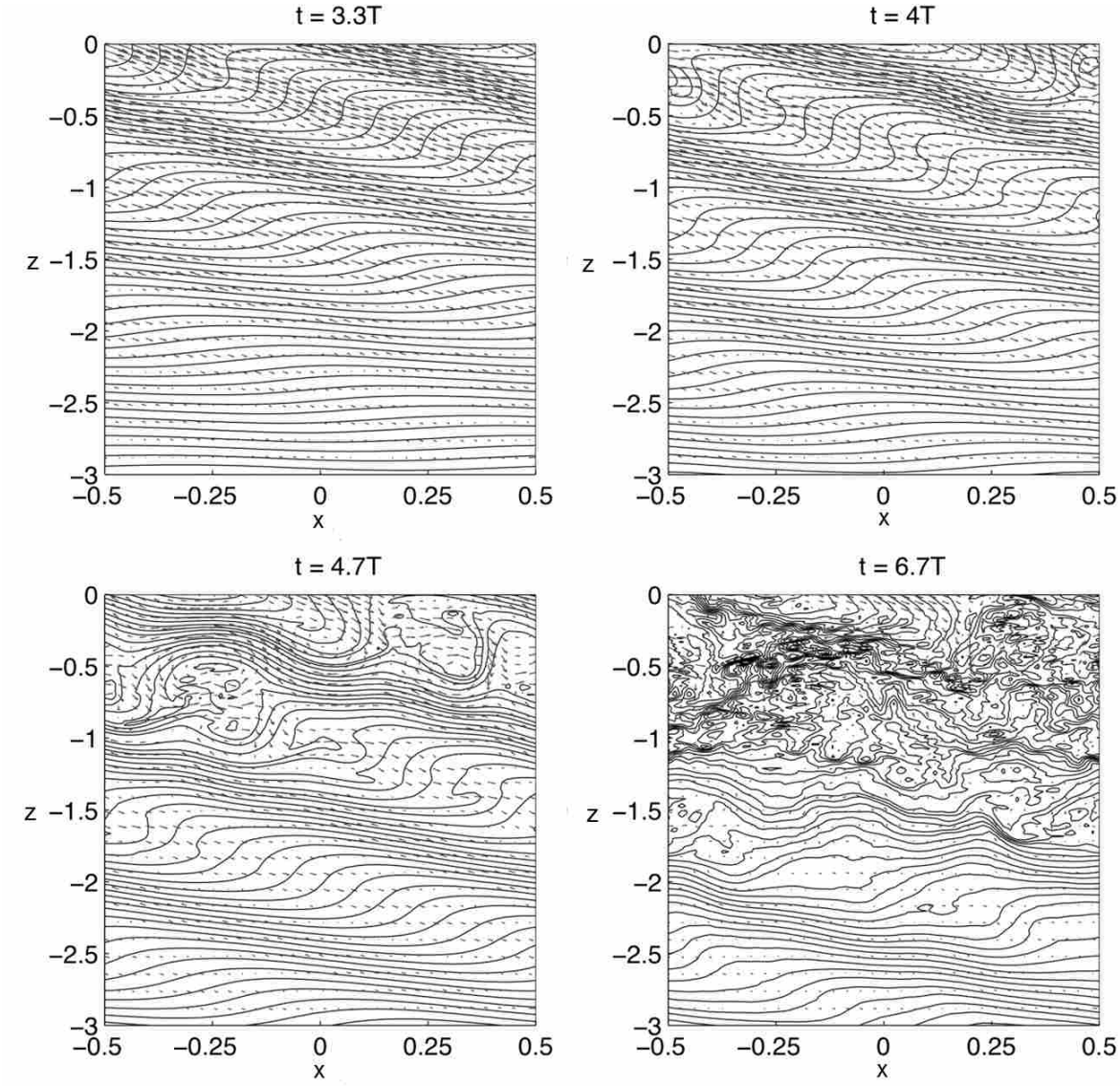

Figure 1.4: These four plots show the evolution in time of a convective instability that grows and results in overturning and wave breaking. At time t=4T (T=inertia periods) the wave begin to overturn while at t=4.7T some of the waves are breaking. Taken from Liu et al. [2]

using a high-resolution non-linear model to examine the interaction between a short wave packet and a mean shear. They showed that if the amplitude of the waves is sufficiently large, the energy of the wavepacket is not transfered to the shear, but is maintained by the short wave packet for several buoyancy periods. As these waves approach the critical level they steepen, overturn and break. During this breaking process energy is lost to turbulence and viscous dissipation. The instabilities leading to wave breaking were parameterized using a gradient Richardson number,

Figure 1.5: This is a Kelvin Helmholtz instability, which occurs when two fluids with different speeds interact and wavelike motions form, which subsequently overturn and break. Shear instabilities affecting the short waves behave very similar to Kelvin Helmholtz instabilities. The inertia wave streches the short wave and induces overturning. Taken from NOAA forecast systems laboratory(http://www-frd.fsl.noaa.gov/mab/scatcat/).

demonstrating that the instabilities were mostly due to shear instabilities. Lombard and Riley [15] performed further research in the subject of instabilities in internal gravity waves interacting with shear flows. Their studies agree with previous work in that internal waves are unstable at any amplitude and that the Richardson number is limited by the critical value of 1/4. In their research Lombard and Riley also found that at low amplitudes, the unstable modes are similar to wave-wave resonance interactions (i.e convective instabilities). In contrast, at larger wave amplitudes, other modes of instability with comparable growth rate appear in different spatial planes making wave instability a three-dimensional problem. In both cases Lombard and Riley found that instability can be linked to the angle of propagation of the wave and that instability gains energy from two routes: instability kinetic energy from interactions with a shear and instability potential energy through the interaction with a wave density field.

Internal gravity waves may also develop instabilities when interacting with large scale inertia waves. During these interactions, the short waves do not behave the same as when encountering a shear flow. Thus it is paramount to understand the effects of time dependence, due to the presence of an inertia wave, on wave instabilities. Sartelet [13] concluded for waves propagating in the same direction, that when the shear is time-dependent, whether or not wave breaking occurs at regions of strong refraction depends on the initial amplitude of the short wave and not on the time-dependence of the shear. Liu. W, Bretherton, Liu. Z, Smith, Rutland. C and Rutland. H [2] utilized

a non-linear pseudo-spectral model, which included a pre-defined local gradient Richardson number to parameterize and separate convective and shear instabilities. From this parameterization Liu, et al. found, consistent with linear theory, that convective instabilities have a maximum between crests and troughs of the inertia wave, where the greatest density perturbations are induced by the wave. On the other hand, shear instabilities had double the maxima around wave troughs and crests saddled by a minimum in the middle.

In a stability analysis of internal waves, it is important to parameterize and identify the presence of shear and convective instabilities. However, it is known from previous work (Winters and D'Asaro [1], Lelong and Dunkerton [16]) that unstable internal waves may propagate for many buoyancy periods before breaking. Therefore, a temporal dependence should be investigated in the instability and wave breaking process. Sutherland [17] analyzed two-dimensional, large-amplitude, non-hydrostatic internal wavepackets analytically and by numerical simulations. He concluded that the breaking condition requires not only that the wave be statically unstable, but also that the convective instability growth rate be greater than the frequency of the waves ($1/\omega < T_{ins}$).

The author of this thesis uses linear and 2d non-linear models similar to the models used by previous researchers mentioned throughout this section to compare and create the best estimate of steepness for convective instabilities. The effects of the time dependence are considered on the dynamics and stability of waves during wave-wave encounters. A stability analysis is performed where shear and convective instabilities are parameterized using a non-dimensional parameter the gradient Richardson number. To include the temporal dependence in the stability analysis, we compared the timescales of the instabilities to the timescales of the short wave. This process concluded with a general idea of waves estimated to break as a function of initial group speed and wave steepness. These estimates can be used to find the internal waves estimated to break from a spectrum of waves.

CHAPTER 2. METHODS

2.1 Idealized problem

The main scenario in this study is that of a small-scale internal wave packet (short wave) propagating through a time-dependent idealized inertial wave (long wave, see figure 2.1). The short wave packet is bounded with a Gaussian envelope containing short waves with high frequencies and scales in the hundreds of meters horizontally and tens of meters in the vertical. The inertia wave has vertical wavelengths that range in the hundreds and horizontal wavelengths in the thousands of meters. The frequency of the inertial wave is equal to the Coriolis frequency and the group velocity ($\vec{C_g}$) of the inertia wave packet is treated as negligible, since k and l (horizontal wavenumbers) are approximately zero. The inertia wave vertical wavenumber is defined as $M = 2\pi/\lambda_z$ where λ_z is the vertical wavelength. The phases of the inertia wave propagate upward with a vertical phase speed $C = \omega/M$ where $\omega = f$ (Coriolis frequency), which is common for the ocean and atmosphere. The inertial wave can be defined as either an infinite wave-train or as a wave packet bounded by an ideal Gaussian envelope, as shown in equation 2.1.

$$U + iV = U_0 e^{-(z/L)^2} e^{i(Mz - ft)}. \tag{2.1}$$

where L is the length-scale of the envelope, U_0 is the maximum horizontal velocity at the center, and z is the vertical location of the packet taken from the center of the envelope. A simplified diagram of the interaction is represented in figure 2.1. Initially the short wave packet and the inertia wave packet are spatially separated and a Cartesian coordinate system is selected as a frame of reference. In this frame of reference (z) is positive upwards and (x, y) are the axes on the horizontal plane. The buoyancy frequency N is assumed to have no spatial or temporal dependence, which is reasonable because in the deep ocean the density does not change significantly with depth. The Coriolis frequency is assumed constant. This frequency is defined as $f = \pi \sin(\phi)$, where ϕ is

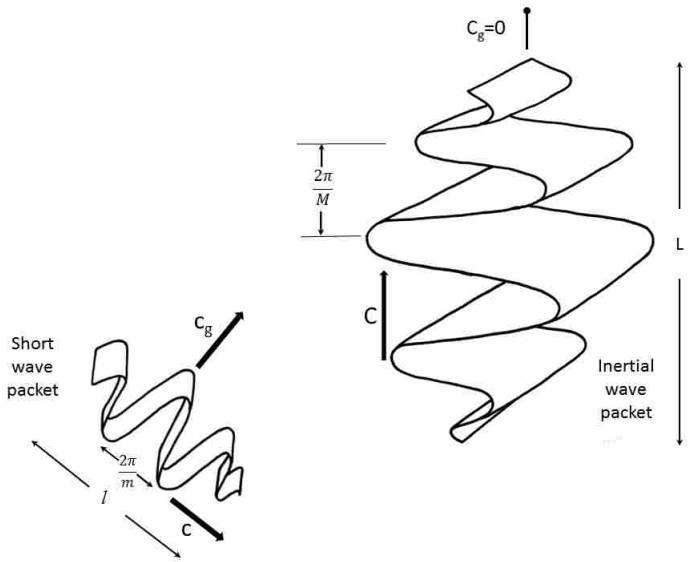

Figure 2.1: This cartoon is a simplified representation of the specific wave-wave interactions researched in this study. The large inertia wave packet is assumed fixed in space with phases propagating upward. The short wave packet is translating towards the large wave packet and its phases are propagating downwards

the latitude. Assuming a constant Coriolis frequency is a reasonable assumption considering the latitude in the interactions modeled does not change drastically. The short wave packet propagates in the vertical and horizontal directions with wavenumbers m and k respectively. Since the short wave packet energy is propagating upwards with respect to depth (z), the vertical wavenumber m is negative. The horizontal wavenumber k is defined positive, thus propagating in the positive (x) direction.

The short wave packet exhibits dispersion during propagation due to enveloping. The equation dictating the wave dispersion of these internal gravity waves will be derived and introduced in more detail later in this section. Appendix A shows a physical representation of wave dispersion and its relationship to the length scale of the wave envelope. The Navier-Stokes equations govern the dynamics of these enveloped short internal waves and are shown by equations 2.2 through 2.5. To simplify the equations it is assumed that the fluid is incompressible and inviscid, which are acceptable assumptions for internal waves studied in the ocean with horizontal and vertical scales

in the hundreds to thousands of meters.

$$\rho \frac{\mathrm{Du}'}{\mathrm{Dt}} = -\frac{\partial p'}{\partial x} + \rho g_x \tag{2.2}$$

$$\rho \frac{\mathrm{Dv}'}{\mathrm{Dt}} = -\frac{\partial p'}{\partial y} + \rho g_y \tag{2.3}$$

$$\rho \frac{\mathrm{Dw}'}{\mathrm{Dt}} = -\frac{\partial p'}{\partial z} + \rho g_z \tag{2.4}$$

$$\frac{\partial u'}{\partial x} + \frac{\partial v'}{\partial y} + \frac{\partial w'}{\partial z} = 0, \tag{2.5}$$

Pressure and density are defined in this particular case as follows: $p = \bar{p} + p'$, where p' is the perturbation pressure and the hydrostatic pressure $\bar{p} = \rho g h$. $\rho = \rho_0 + \bar{\rho} + \rho'$, where ρ' is the perturbation density, ρ_0 is a reference density and the average density ($\bar{\rho} = f(z)$) is a function of elevation. From these definitions of pressure and density and doing a small-particle force balance, the buoyancy frequency N can be derived as follows.

If a particle in a stratified fluid is displaced from its equilibrium position as seen in figure 1.1 buoyancy and gravitational forces will act on it. Summing the forces generating the particle acceleration, assuming the fluid is incompressible and knowing that ζ_0 is a small amplitude perturbation, yields:

$$m\frac{\partial^2 \zeta}{\partial t^2} = \rho_1 g \forall - \rho_0 g \forall. \tag{2.6}$$

Since $m = \rho_0 \forall$, the terms ($\forall$) in equation 2.6 cancel out. Solving for $\partial^2\zeta/\partial t^2$ yields.

$$\frac{\partial^2 \zeta}{\partial t^2} = \left(\frac{\rho_1 - \rho_0}{\rho_0}\right) g. \tag{2.7}$$

Expanding ρ_1 about ρ_0 using a Taylor's series yields $\rho_1 = \rho_0 + \zeta(d\rho/dz) +$ higher order terms. Using the the Taylor's expansion in equation 2.7, results in a partial differential equation of the form:

$$\frac{\partial^2 \zeta}{\partial t^2} - \left(\frac{\mathrm{d}\rho}{\mathrm{dz}}\frac{g}{\rho_0}\right)\zeta = 0. \tag{2.8}$$

Solving the differential equation presented above, results in the following solution form.

$$\zeta = ae^{i\left(-\frac{\mathrm{d}\rho}{\mathrm{dz}}\frac{g}{\rho_0}\right)^{\frac{1}{2}}t} + be^{-i\left(-\frac{\mathrm{d}\rho}{\mathrm{dz}}\frac{g}{\rho_0}\right)^{\frac{1}{2}}t}, \tag{2.9}$$

where the characteristic roots of this equation become the definition of the buoyancy frequency (natural frequency of the fluid).

$$N^2 = -\frac{\mathrm{d}\rho}{\mathrm{dz}}\frac{g}{\rho_0}. \tag{2.10}$$

The Boussinesq approximation is used to simplify the governing equations and it states that the density perturbations ρ' are small relative to the reference density ρ_0. Hence ρ' is only important when multiplied by gravity. This approximation is reasonable for ocean waves because the density does not change significantly with respect to depth. Employing this approximation and assuming $\rho' D\vec{u'}/Dt$ is approximately $\rho_0 D\vec{u'}/Dt$, the momentum equations become:

$$\frac{\partial u'}{\partial t} + u'\frac{\partial u'}{\partial x} + v'\frac{\partial u'}{\partial y} + w'\frac{\partial u'}{\partial z} = -\frac{1}{\rho_0}\frac{\partial p'}{\partial x} \tag{2.11}$$

$$\frac{\partial v'}{\partial t} + u'\frac{\partial v'}{\partial x} + v'\frac{\partial v'}{\partial y} + w'\frac{\partial v'}{\partial z} = -\frac{1}{\rho_0}\frac{\partial p'}{\partial y} \tag{2.12}$$

$$\frac{\partial w'}{\partial t} + u'\frac{\partial w'}{\partial x} + v'\frac{\partial w'}{\partial y} + w'\frac{\partial w'}{\partial z} = -\frac{1}{\rho_0}\frac{\partial p'}{\partial z} + \frac{\rho'}{\rho_0}g_z \tag{2.13}$$

$$\frac{\mathrm{d}\rho}{\mathrm{dt}} = 0 = \frac{\partial \rho}{\partial t} + u'\frac{\partial \rho}{\partial x} + v'\frac{\partial \rho}{\partial y} + w'\frac{\partial \rho}{\partial z} = \frac{\partial \rho'}{\partial t} + w'\frac{d\bar{\rho}}{\partial z}, \tag{2.14}$$

The equations are linearized, assuming that u', v', and w', are small and any products of these terms will be removed from the equations.

$$\frac{\partial u'}{\partial t} = -\frac{1}{\rho_0}\frac{\partial p'}{\partial x} \tag{2.15}$$

$$\frac{\partial v'}{\partial t} = -\frac{1}{\rho_0}\frac{\partial p'}{\partial y} \tag{2.16}$$

$$\frac{\partial w'}{\partial t} = -\frac{1}{\rho_0}\frac{\partial p'}{\partial z} - \frac{\rho'}{\rho_0}g_z \tag{2.17}$$

$$\frac{\partial \rho'}{\partial t} + w'\frac{d\bar{\rho}}{\partial z} = 0, \tag{2.18}$$

These are referred to as the linear Boussinesq equations. These equations can be rearranged to relate all of them to w' to find the perturbation density, pressure, and particle velocities. These expressions are the polarization relations which are included in Appendix B.

The derivation of the dispersion relation (intrinsic frequency of the short waves, equation 2.19) is presented in Appendix C.

$$\omega^2 = \frac{N^2\left(k^2+l^2\right)+f^2m^2}{k^2+l^2+m^2}. \tag{2.19}$$

In the particular interactions studied in this research $l = 0$ for the short waves or in other words, the short waves are two-dimensional. If the intrinsic frequency (ω) of the short wave is assumed to be much higher than the Coriolis frequency but much lower than the buoyancy frequency, the dispersion relation 2.19 can be simplified in the following manner:

$$\omega^2\left(k^2+m^2\right) = N^2k^2+f^2m^2. \tag{2.20}$$

$$\left(\omega^2-N^2\right)k^2 = \left(f^2-\omega^2\right)m^2. \tag{2.21}$$

Since ω is much greater than f then $f^2-\omega^2 \approx -\omega^2$. On the other hand since ω is much smaller than N then $\omega^2-N^2 \approx -N^2$. Using these simplifications on expression 2.21 yields:

$$\omega = \frac{\mathrm{Nk}}{m}. \tag{2.22}$$

One important parameter in this study, in particular for the stability analysis, is the steepness. The steepness is defined as the difference of the vertical displacement ζ with respect to depth z. Figure 2.2 shows lines of constant density (isopycnals) from which steepness can be found by calculating the vertical displacement with respect to depth or the slope of the isopycnals. In the numerical simulations performed for this research, a vertical displacement field is initialized at time $t = 0$ which is of the form:

$$\zeta(x,z,0) = \mathrm{Re}\left\{\zeta_0 e^{\frac{-(z-z_0)^2}{b^2}} e^{i(kx+mz)}\right\}. \tag{2.23}$$

The real part of this expression is used to describe the vertical displacement field. In equation 2.23, b is the length scale of the short wave packet and z_0 is the initial position of the short wave packet.

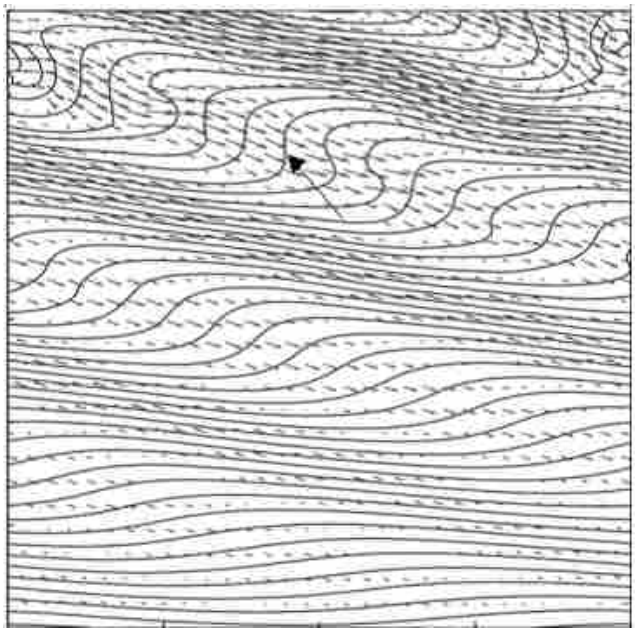

Figure 2.2: Lines of constant density (isopycnals) with a vertical slope as signaled by the black arrow. Once the isopycnals become vertical a state of static instability develops and overturning may occur. However this instability has to last long enough to evolve into a breaking wave. Taken from Liu et al. [2].

2.2 2D Non-linear model

The 2D non-linear model is used in this study as a basis of comparison and to test the validity of the amplitude estimates found in the ray theory (linear theory). Since the main interest of this research is to analyze instabilities, which are non-linear, a non-linear model is imperative. However, the non-linear model is limited to small initial amplitudes because breaking, an adverse effect of large initial amplitudes, is undesirable since the non-linear model is two dimensional. In addition, by preventing wave breaking, measures of wave steepness changes are captured providing more information about wave instabilities and breaking in the non-linear model being used. The non-linear model is governed by the Navier-Stokes equations in their vorticity-stream form. In this model the stream function is defined as follows:

$$u' = -\frac{\partial \psi}{\partial z}. \tag{2.24}$$

$$w' = \frac{\partial \psi}{\partial x} \tag{2.25}$$

The velocity field has components in the horizontal and vertical directions such that $u = (u', 0, w')$. To simplify the equations of motion the fluid is assumed incompressible, inviscid and the Boussinesq approximation is employed. After applying these simplifications, the governing equations are reduced to the following form.

$$\frac{\partial^2 \psi}{\partial x^2} + \frac{\partial^2 \psi}{\partial z^2} = -q \tag{2.26}$$

$$\frac{\partial q}{\partial t} + J(\psi, q) - \frac{\partial \sigma}{\partial x} - f\frac{\partial v}{\partial z} = 0 \tag{2.27}$$

$$\frac{\partial v}{\partial t} + J(\psi, v) + fu = 0 \tag{2.28}$$

$$\frac{\partial \sigma}{\partial t} + J(\psi, \sigma) - N^2 w = 0, \tag{2.29}$$

where q is the y-component of vorticity and $J(\psi, q)$ is the Jacobian with respect to (x, z). In these equations $\sigma = g\rho'/\rho_0$ is the reduced gravity term, where g is the gravitational constant and ρ' is the density perturbation. The equations of motion (2.26)-(2.29) are solved using forth order Runge-Kutta schemes inside a time stepping loop. The boundary conditions imposed on the equations are periodic in the x and z directions. The grid is defined by 512 points in the vertical direction and 16 points in the horizontal. The size of the domain is specified as follows: The vertical limit is chosen to fit the wave-wave interaction. The horizontal limit corresponds to the horizontal wavelength of the short wave. This model has been validated for time spacing and and grid spacing with previous test at higher resolution and smaller time-steps between a short internal wave interacting with a steady shear and satisfactory results where attained. The model and its validation is described in Vanderhoff et al. [10].

The vertical displacement is used to define the steepness which is the main parameter used to study instabilities. In figure 1.1 the slope of the density gradient is defined as $\partial z/\partial \rho$ which is equivalent to $\partial z/\partial \rho = \zeta/\rho'$. Substituting this relationship into equation 2.10 and solving for ζ gives an expression for the vertical displacement.

$$\zeta = \frac{\rho' g}{N^2 \rho_0}, \tag{2.30}$$

The steepness is calculated from the vertical displacement equation 2.30 by taking the partial derivative of the vertical displacement with respect to z.

$$\zeta_z = \frac{\partial \zeta}{\partial z} = \frac{g}{N^2 \rho_0} \frac{\partial \rho'}{\partial z}, \tag{2.31}$$

2.3 Linear model

2.3.1 Ray equations

The linear model (ray theory) is used along with the dispersion relation for simulating internal waves and internal wave interactions. In ray theory, internal waves or internal wave packets are simplified and simulated as rays following the energy path of the wave, where the wavenumbers, frequency, and group velocity are known to follow the energy only, though the individual particle velocities are ignored. The ray equations describing the internal waves are given by expressions 2.32 and 2.33.

$$\frac{D\vec{K}}{Dt} = -\frac{\partial \omega}{\partial \vec{x}} + \vec{U}\vec{K} \tag{2.32}$$

$$\vec{c_g} = \frac{D\vec{x}}{Dt} + \vec{U}. \tag{2.33}$$

With these equations and the dispersion relation, 2.19, it is possible to simulate internal waves through a background flow field. These equations are derived in the appendix D.

The ray equations 2.32 and 2.33 are discretized and a numerical model is developed in MATLAB, which solves the equations using a fourth order Runge-Kutta method.

It is important to emphasize that ray tracing model uses linear WKBJ theory to calculate the dynamic properties of the internal waves as they propagate through other flows. The WKBJ approximation includes the following assumptions: the interaction of the small wave does not affect or change the background flow field, the buoyancy frequency is constant, fluid viscosity is neglected and the WKBJ approximation is valid prior to wave breaking or inflection. Hence the wavenumbers and frequency of the short wave are slowly varying.

2.3.2 Hayes equations

The amplitude of the short-waves must be calculated directly from a ray-tracing integration. To do this a set of equations called the Hayes equations (See [18]) are used to relate the volume of ray tubes (tubular surface made up of rays) to the amplitude (a) of the waves represented by the ray tubes. One parameter used in this process is the wave action density, which is a relationship between wave energy density over the wave frequency ($A_d = E/\omega$).

In its simplest relevant form the ray equation for the wave action density, where A_d is the amplitude square, is

$$\frac{\mathrm{dA}_d}{\mathrm{dt}} = -A_d \frac{\partial c_g}{\partial z} = -A_d \left(G_{\mathrm{mm}} \frac{\partial m}{\partial z} + G_{\mathrm{mz}} \right), \tag{2.34}$$

where $d/dt = \partial/\partial t + \vec{c_g}\partial/\partial z$, $G(m,z,t) = \omega(z,t)$ and $G_{mz} = 0$. The value of $\partial m/\partial z$ in 2.34 is calculated from a numerical integration of

$$\frac{d}{\mathrm{dt}} \left(\frac{\partial m}{\partial z} \right) = \frac{\partial}{\partial z} \left(\frac{\mathrm{dm}}{\mathrm{dt}} \right) - \frac{\partial c_g}{\partial z} \frac{\partial m}{\partial z} = -G_{\mathrm{zz}} - G_{\mathrm{mm}} \left(\frac{\partial m}{\partial z} \right)^2, \tag{2.35}$$

The notation G_{ii} refers to the second partial derivative of G with respect to i. The parameter $\partial m/\partial z$ indicates the local degree of focusing in a bundle of rays, which vanishes when the rays are parallel in (z, t) and diverges at a caustic (Regions of strong refraction).

For this analysis it is important to understand that the wave action is constant across the ray tubes, A =constant. Thus, if the wave action density is integrated across the ray volume the following expression is obtained

$$\int A_d \, d\forall = \text{cst along ray}. \tag{2.36}$$

From this integration the following relationship can be set

$$\frac{\forall_0}{\forall} = \frac{A_d}{A_{d_0}}. \tag{2.37}$$

Hence, in the amplitude approximations near caustics, one is interested in the changes of the ray tube volume with respect to a reference initial volume ($\forall_0/\forall$).

Equations 2.34 and 2.35 are modified by using the wave action (A_d), which is related to the volume of the rays such that $\forall = 1/A_d$. In addition if the vertical wavenumber and depth of the ray path are written as functions of time and initial position z_0 equations 2.34 and 2.35 become

$$\frac{d\forall}{\mathrm{dt}} = \forall G_{\mathrm{mm}} \frac{\partial m}{\partial z} \tag{2.38}$$

$$\frac{d}{\mathrm{dt}}\left(\frac{\partial z}{\partial z_0}\right) = G_{\mathrm{mm}} \frac{\partial m}{\partial z_0} \tag{2.39}$$

$$\frac{d}{\mathrm{dt}}\left(\frac{\partial m}{\partial z_0}\right) = -G_{\mathrm{zz}} \frac{\partial z}{\partial z_0}, \tag{2.40}$$

with

$$\frac{\partial m}{\partial z} = \frac{\partial m / \partial z_0}{\partial z / \partial z_0}. \tag{2.41}$$

These are the equations proposed by Hayes, who recognized their practical value when dealing with caustics (Regions of strong refraction where closely spaced rays intersect). The integration of equations 2.38 through 2.40 gives a sign change in the variable $\forall$ after the ray intersects a caustic. Hence A_d can become negative. To keep the wave action density positive the relationship between the volume of the ray tube and the amplitude is modified

$$A_d = \frac{1}{|\forall|} \tag{2.42}$$

The volume of the ray tube vanishes at caustics and thus the amplitude of the short wave is a singularity. This result is not insightful to the stability analysis because steepness which is derived from the amplitude will also be a singularity. These singularities at caustics are the result of the linear theory (ray theory) failing because the amplitude and wavenumber of the short wave are not slowly varying. Nonetheless, in the next section a more accurate estimate of the amplitude is developed which can be used for stability analysis.

2.3.3 Caustics

Caustics are regions of strong refraction where closely spaced rays intersect, hence making the volume of the tubular surface composed of these rays vanish (see figure 2.3). In addition at

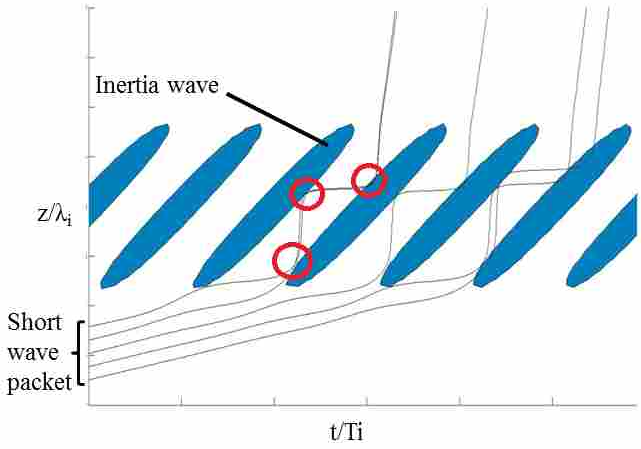

Figure 2.3: Simulation performed using ray tracing of a short wave interacting with an inertia wave. The circled regions are caustics where closely spaced rays intersect and singularities to the amplitudes of the wave occur.

these regions of strong refraction short wave properties such as amplitude and wavenumber are not slowly varying which is one of the conditions necessary to simplify the governing equations in ray theory. Recalling that the amplitude of the wave is related to the ray tube volume by equation 2.42, one notices that the amplitude may become a singularity when the volume ($\forall$) of the ray tube vanishes. A practical solution to estimate the amplitude at caustics is necessary and it is obtained by combining the ray solution (ϕ_r) with an Airy function (ϕ_b) to form a valid result as seen in Broutman and Young [3] and in Peregrine and Smith [19]. The Airy function is selected because it resembles the ray solution very well near the caustic but it does not diverge as the ray solution does. These solutions can be seen in figure 2.4 below. The solution $\phi_r = ae^{i(\alpha)\pm\pi/4}$ is obtained by integrating the steady-state ray equations

$$\frac{\partial m}{\partial z} = -\frac{\Omega_z}{\Omega_m}, \tag{2.43}$$

for m, and

$$\frac{\partial \alpha}{\partial z} = m, \tag{2.44}$$

for α. Ω in equation 2.43 is defined for a steady background current U as $\Omega = \omega + \mathrm{kU}$. The integration begins at the caustic with initial conditions z_c and m_c, which are the location of the

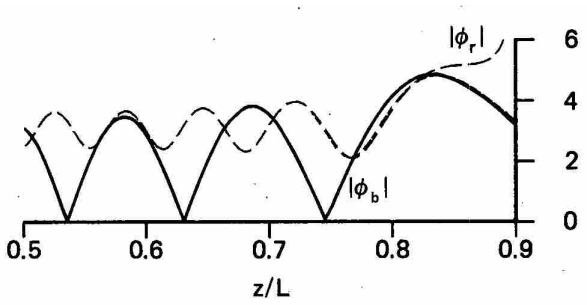

Figure 2.4: The wave solutions obtained from ray theory and the Airy function are contrasted in this figure. Notice that close to the caustic at z/L≈0.8 the Airy function (ϕ_b) resembles the ray solution (ϕ_r) except it does not diverge. Taken from Broutman, D. [3]

caustic and the vertical wavenumber of the short waves at the caustic. This vertical wavenumber is defined as

$$m_c = -\left(\frac{\mathrm{Nk}}{c}\right)^{1/2}. \tag{2.45}$$

To avoid the caustic singularity in equation 2.43 the first integration step is taken analytically using

$$\Omega_m \approx (m - m_c)\,\Omega_{\mathrm{mm}}, \tag{2.46}$$

where Ω_{mm} is evaluated at the caustic. From 2.43 and 2.46

$$m - m_c \sim \pm\left(|z_c - z|\right)^{1/2}\left(\left|\frac{2\Omega_z}{\Omega_{\mathrm{mm}}}\right|\right)^{1/2} \tag{2.47}$$

To obtain the equation for the short wave amplitude valid near the caustic the operator expansion technique outlined in Peregrine and Smith [19] is employed. Following their derivation, a model equation is developed for the short wave amplitude starting from an equation of the type

$$H(\omega, K, z) = \omega - \Omega(K, z), \tag{2.48}$$

where ω is the dispersion relation. H may be expanded about its value at the caustic to obtain

$$H = (z - z_c)\,H_z + \frac{1}{2}(m - m_c)^2 H_{\mathrm{mm}} + \ldots \tag{2.49}$$

where H_z and H_{mm} are evaluated at the caustic, to which it is assigned the vertical wavenumber m_c and the depth z_c. The term H_m does not appear in equation 2.49 because it vanishes at the caustic. The expansion shown in 2.49 is substituted into the Fourier transformed wave equation

$$Hae^{\mathrm{i}\alpha} = 0 \tag{2.50}$$

with

$$ima \approx im_c a + \frac{da}{dz} \tag{2.51}$$

to yield the Airy function governing the envelope of the short waves near the caustic

$$\frac{d^2a}{\mathrm{dz}^2} - (z - z_c)\left(\frac{2H_z}{H_{\mathrm{mm}}}\right)a = 0 \tag{2.52}$$

The solution to equation 2.52 is

$$\phi_b = A_0 \mathrm{Ai}(\delta) e^{\mathrm{im}_c(z-z_c)}, \tag{2.53}$$

where $\delta = (z - z_c)(2\Omega_z/\Omega_m m)^{1/3}$. The constant A_0 is found from matching $\phi_r = ae^{i\alpha \pm \pi/4}$ with equation 2.53. This is accomplished using

$$a \approx B^{1/2}\left(\left|2\Omega_z \Omega_{\mathrm{mm}}^2\right|\right)^{-1/6}(-\delta)^{-1/4}, \tag{2.54}$$

for the ray solution, and

$$\mathrm{Ai}(\delta) \approx -\pi^{-1/2}(-\delta)^{-1/4}\sin\left[\frac{2}{3}(-\delta)^{-1/4} + \frac{\pi}{4}\right] \tag{2.55}$$

for the Airy function. Equation 2.55 is valid as $\delta \to \infty$. On the other hand equation 2.54 is valid as $\delta \to 0$ and it is derived from 2.47 using $B = \Omega_m a^2$. The result of the matching is

$$A_0 = (\pi \mathrm{B})^{1/2}\left(\left|\frac{32}{\Omega_{\mathrm{mm}}^2 \Omega_z}\right|\right)^{1/6}. \tag{2.56}$$

Using the mid-frequency approximation (equation 2.22) the expression for A_0 becomes

$$A_0 = \left(\frac{2\pi \mathrm{B}}{Nk}\right)^{1/2} \mathrm{Ri}_c{}^{1/12} \left|m_c\right|, \tag{2.57}$$

where Ri_c is the value of the Richardson number at the caustic defined as

$$Ri_c = \frac{N^2}{U_z C^2}, \tag{2.58}$$

where U_z is the partial derivative of the velocity profile of the background, equation 2.1,with respect to depth.

This expression for the wave action density is derived for the case when the background is an infinite wave-train. However it is expected that equations 2.56 and 2.57 will make reasonable approximations in the case when the background inertial wave is bounded by a Gaussian envelope, as long as the wave action flux (B) and the total frequency (Ω) vary slowly across the envelope length-scale. Further simplification to equation 2.57 can be accomplished when the refraction is strong enough to make $|m| \gg |m_c|$ on one side of the caustic, which is noticed when the short wave approaches with a group speed slower than the phase speed of the inertia wave and with a group speed faster than the phase speed of the inertia wave. During these two scenarios the conservation of wave-action flux ($B = (c_g - C)A$) forces A to be approximately constant. Let this constant value be A^*. Substituting $B \approx CA^*$ into equation 2.57 and using definition 2.45, a relationship between A^* and the caustic amplitude A_0 is found such

$$A_0 = (2\pi)^{1/2} \mathrm{Ri}_c{}^{1/12} (A^*)^{1/2}. \tag{2.59}$$

The value of the amplitude at the caustic (A_0) depends on the local Richardson number at the caustic (Ri_c) and A^* which is the value of A away from the caustic in the direction along the short wave ray of decreasing vertical group speed c_g.

2.3.4 Steepness

The steepness is a parameter of interest in the stability analysis because when $\zeta_z > 1$ waves are vertical and estimated to develop convective instabilities leading to breaking. This parameter is derived in linear theory using the definition of potential energy found in Pedlosky [20], modified to include the influence of the inertia frequency f, and the dispersion relation equation 2.19. The energy for internal waves with vertical displacement $\zeta = \zeta_0 e^{i\theta}$ is,

$$E = \frac{1}{2}\rho_0 {\zeta_0}^2 N^2 \left[1 + \left(\frac{\mathrm{fm}}{\mathrm{Nk}}\right)^2\right], \tag{2.60}$$

where ρ_0 is the reference density. Solving for ζ_0 in equation 2.60, substituting $A = E/\omega$ and utilizing the assumptions used for the mid-frequency approximation (i.e. $\omega \ll N$ and $f \ll \omega$), an expression can be derived for the vertical displacement as a function of wave energy

$$\zeta_0 = \left[\frac{2A\omega}{\rho_0 N^2}\right]^{1/2}. \tag{2.61}$$

Recalling equation 2.30 and taking the partial derivative of this expression with respect to z gives a relationship between the maximum steepness and initial vertical displacement $\zeta_{zmax} \approx |\mathrm{m}\zeta_0|$. Equation 2.61 is multiplied by m, then rearranging and noting that $m^2/N^2k^2 = 1/\omega^2$ for the mid-frequency approximation, the steepness in the linear model is

$$\zeta_z = k\left(\frac{2A}{\omega\rho_0}\right)^{1/2}, \tag{2.62}$$

which is applicable only within the mid-frequency approximation.

2.4 Stability analysis

The stability analysis is carried out for three different types of wave-wave interactions. All of these interactions are defined according to the relationship between the group speed of the short wave (c_g) relative to the phase speed of the inertia waves (C). Thus, first kind encounters are characterized by short waves approaching with group speeds greater than the phase speed of the inertia wave. Second kind encounters are those with short waves approaching with group speeds

approximately equal to the phase speed of the inertia wave, while third kind encounters feature short waves with group speeds slower than the phase speed of the inertia wave.

It is important to mention that a linear model is being used to estimate instabilities which are a non-linear phenomenon. Consequently, the use of approximations to estimate instabilities are necessary. The linear model though, provides insight which leads to estimates of waves that are expected to break. The 2D non-linear model is able to capture the onset of instabilities but not the actual wave breaking. Thus, no estimates of breaking scales, or the extent of the breaking are included in this study.

The stability analysis of this research begins with the steepness parameters found from the non-linear and linear models, equations 2.62 and 2.31 respectively. The steepness is an important variable because it will be used to parameterize convective instabilities detected in the short waves. Convective instabilities occur when the propagating waves refract and subsequently develop large vertical displacements relative to depth equal to and greater than unity ($\zeta_z \geq 1$). These large vertical displacements induce lines of constant density to become vertical, overturn and break. This instability is illustrated in figure 2.2 where the lines are the isopycnals and the arrow is pointing to the line with a steepness equal to and greater than one (Taken from Liu et al. [2]).

The second variable important to the stability study is the total shear from the inertia wave, which has the following form

$$\frac{dU}{dz} = \frac{\partial U}{\partial z} + \frac{\partial U}{\partial t}\frac{1}{C}. \tag{2.63}$$

This expression describes mathematically the characteristics of the shear from the inertia wave and it parameterizes the shear instabilities caused by the presence of the inertia wave. Shear instabilities occur when the short waves are subjected to the shear due to the inertia wave. The amplitude of the short wave increases, and its frequency and wavenumber approach zero, which may result in wave breaking as shown in previous studies by Winters and D'Asaro [1], Lombard and Riley [15] and Desaubies and Smith [21]. Both of the parameters mentioned above, steepness and total shear, are combined into a single expression called the gradient Richardson number derived as follows.

Starting from the definition of the gradient Richardson number found in earlier works

$$\mathrm{Ri}_g = \frac{\mathrm{Ri}\left(1 - \frac{\mathrm{d}\rho'}{\mathrm{dz}}\right)}{\left(\frac{\mathrm{dU}}{\mathrm{dz}}\right)^2}. \tag{2.64}$$

Non-dimensionalizing 2.64 gives.

$$\mathrm{Ri}_g = \frac{\left(\frac{\mathrm{NL}}{U}\right)^2 \left(1 - \frac{\mathrm{d}}{\mathrm{dz}}\left[\frac{\rho'}{L|\mathrm{d}\rho/\mathrm{dz}|}\right] L\right)}{\left(\frac{\mathrm{dU}}{\mathrm{dz}}\right)^2 \left(\frac{L}{U}\right)^2}. \tag{2.65}$$

Employing the chain rule knowing that that $d\rho/dz$ is not a function of z yields

$$\mathrm{Ri}_g = \frac{N^2 \left(\frac{L}{U}\right)^2 \left(1 - \frac{\partial \rho'}{\partial z}\left[\frac{1}{|\mathrm{d}\rho/\mathrm{dz}|}\right]\right)}{\left(\frac{\mathrm{dU}}{\mathrm{dz}}\right)^2 \left(\frac{L}{U}\right)^2}. \tag{2.66}$$

Substituting equation 2.10 for $d\rho/dz$ and equation 2.31 for $\partial\rho'/\partial z$ makes the gradient Richardson become

$$\mathrm{Ri}_g = \frac{N^2 (1 - \zeta_z)}{\left(\frac{\mathrm{dU}}{\mathrm{dz}}\right)^2}, \tag{2.67}$$

where the denominator dU/dz is the total derivative defined by equation 2.63 and ζ_z is the steepness. The gradient Richardson number will specify if a wave field is unstable when a critical threshold of $1/4$ is surpassed.

$$\mathrm{Ri}_g = \frac{N^2 \left(1 - \frac{\partial \zeta}{\partial z}\right)}{\left(\frac{\mathrm{dU}}{\mathrm{dz}}\right)^2} < \frac{1}{4}. \tag{2.68}$$

If the gradient Richardson number is separated into an angle following the method outlined in Winters and D'Asaro [1], convective and shear instabilities can be identified.

$$\theta = \tan^{-1}\left[\frac{\frac{1}{4}\left(\frac{\mathrm{dU}}{\mathrm{dz}}\right)^2}{N^2\left(1 - \frac{\partial \zeta}{\partial z}\right)}\right]. \tag{2.69}$$

This angle will fall into one of three stability regions: stable, shear unstable, or purely convectively unstable. Thus, providing specific information about the type of instability.

It is important to know as well the temporal relationship between shear or convective instabilities and wave breaking. As mentioned in the introduction, Sutherland [17] proposed that the temporal dependence of instabilities must be included in an analysis of stability. The wave must be unstable for long enough to have time to grow and cause the waves to overturn and break. This hypothesis is based on the assumption that wave-wave resonant interactions amplify short waves in

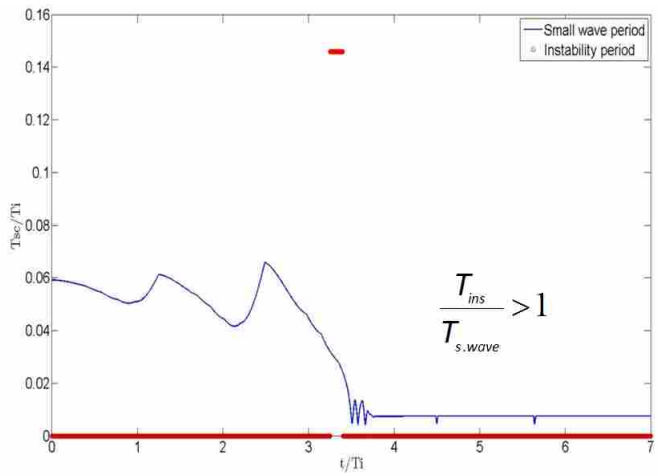

Figure 2.5: Magnitude of the timescale of the instability plotted in red circles and magnitude of the timescale of the short wave plotted in blue solid line. These two magnitudes are compared at the same time interval when the instability is captured. If the timescale of the instability is larger than the timescale of the short wave, breaking is estimated to occur.

both the linear and non-linear regimes, which has been proven before by Grimshaw in 1977 [22]. Therefore, a practical expression to compare the timescales of the instability to the timescale of the short wave is necessary. This relationship is presented in equation 2.70 and it is also shown graphically in figure 2.5. In this figure the magnitude of the timescale of the instability is represented by the circles. Note that the magnitude of the instability timescale is greater than the magnitude of the timescale of the short wave (solid line) during the time interval when the instability occurred.

$$\frac{T_{\text{ins}}}{T_{s.\text{wave}}} > 1, \tag{2.70}$$

where T_{ins} is the timescale of the instability defined as the length of time (Δt) the instability persisted, normalized by the inertia period ($T_i = 2\pi/f$) or

$$T_{\text{ins}} = \frac{\Delta \text{t}}{T_i}, \tag{2.71}$$

and $T_{s.\text{wave}}$ is the timescale of the short wave defined as the period of the short wave, normalized by the inertia period or

$$T_{s.\text{wave}} = \frac{1}{\omega T_i}. \tag{2.72}$$

Notice that equation 2.70 is coupled to an inequality. When the timescale of the instabilities is larger than the timescale of the short wave, it is estimated that the instabilities persisted long enough for wave breaking to occur.

CHAPTER 3. RESULTS

3.1 Validation of the Airy function amplitude approximations

Using the 2d non-linear model the interaction between an inertia wave with phases propagating upwards and a short wave propagating upwards is developed. This interaction is shown in figure 3.1(a) and 3.1(b). Figure 3.1(a) is the shear (dU/dz) from the inertia wave. Each black and white successive elliptical region in this plot represents a phase of the inertia wave. Notice how the ellipses fade near the upper and lower limits. This is an effect of the envelope surrounding the wave. The slope of these regions depict the inertia wave phases propagating upwards with a vertical wavelength of 75 m. The length-scale of the inertia envelope (L) is chosen to be 35 m, which results in one full wavelength in the envelope. The maximum velocity of the inertia wave is $U_0 = 0.02$ m/s and the envelope of the inertia wave is centered in the middle of the computational domain. Figure 3.1(b) presents the density perturbation field, which only corresponds to the short wave since the inertia wave has no vertical displacement. In this particular case the short wave is propagating towards the inertia wave at a group speed slower than the phase speed of the inertia wave. This short wave characteristic can be seen by shallower slopes in the motion of the short wave relative to the slopes of the inertia wave. This type of interaction ($c_g < C$) has been previously defined by other authors and it is known as a third kind encounter (See Vanderhoff et al. [10] and Broutman et al. [23]). Note the short wave packet is initialized at a depth below the inertia wave as seen in figure 3.1(b). This is done to make sure the short wave is not interacting with the inertia wave when the simulation begins. If this practice is not followed carefully the short wave is not resolved in the early times of the simulation and comparisons with ray theory are marginalized.

The simulation performed using the non-linear model is replicated as closely as possible using the linear model (ray tracing). This step in the stability analysis is necessary to validate qualitatively and quantitatively the results from the linear approximations. To duplicate the interactions all the parameters for both waves are matched and set equal. Figure 3.1(c) is the ray tracing

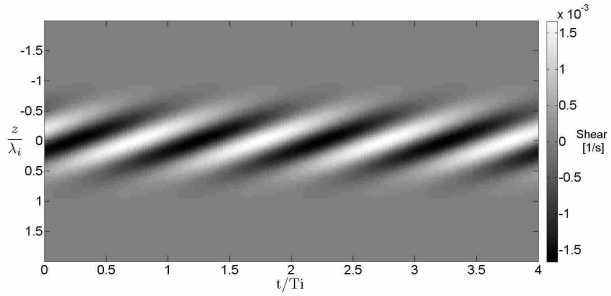

(a) Inertia shear that the small-scale wave encounters.

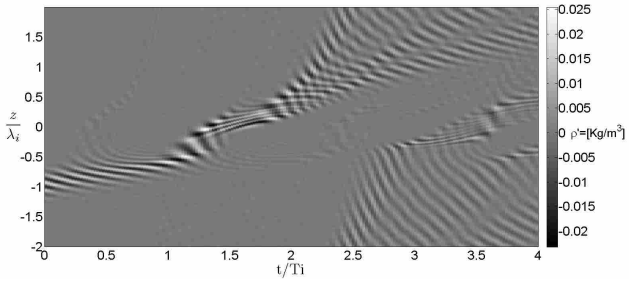

(b) Vertical displacement field (steepness), which portrays how the short wave packet propagates upwards toward the inertia wave.

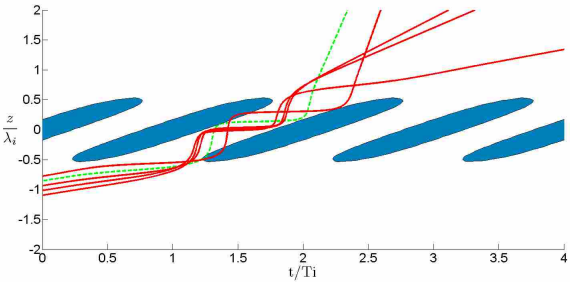

(c) Ray tracing representation of the same interaction simulated with the 2d non-linear model shown in figure 3.1(b).

Figure 3.1: The set of rays represent the short wave packet approaching the inertia wave. The blue ellipses approximate the inertia wave location and they are outlined by the condition $c_{gz0} = C$ where caustics are observed. The short wave packet in this instance propagates with a group velocity lower than the phase speed of the inertia wave.

approximation to the encounter portrayed in figure 3.1(b). Figures 3.2(a) and 3.2(b) represent a first kind encounter simulated using the non-linear model and replicated using ray tracing. There is wave dispersion which occurs in the non-linear model simulations, but it is not observed in the ray tracing plots. This dispersion due to waves of different frequencies traveling at different group velocities is explained in detail in Appendix A. It is important to choose an encounter from the non-

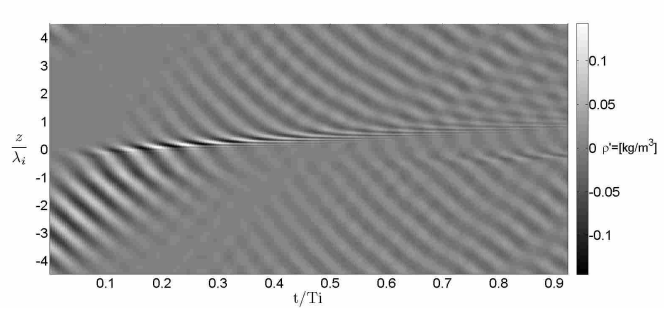

(a)

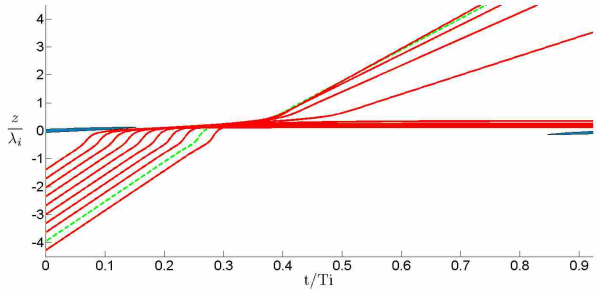

(b)

Figure 3.2: Simulation performed using both models of a short wave approaching the same inertia wave as in figure 3.1(a) with a group speed greater than the phase speed of the inertia wave ($c_g > C$).

linear simulations that shows the short wave refracting almost in its entirety in a single phase of the inertia wave to make the numerical simulations and ray theory simulations more comparable and thus the adjusted amplitude estimates more accurate. The simulations will never be exact though, because the non-linear model exhibits more realistic energy dispersion than the linear theory.

The two pairs of figures 3.3(a)-3.3(b) and 3.4(a)-3.4(b) present a specific case comparing the maximum steepness from non-linear simulations and that found from ray tracing. The maximum steepness in the non-linear simulation is found within the entire domain at each time step and is normalized by the initial steepness. Notice on figures 3.1(c) and 3.2(b) that the wave-packet in ray tracing is represented by a group of rays. Each of those rays has an individual steepness, but a single ray is chosen (highlighted green line in figures 3.1(c) and 3.2(b)) with a steepness comparable to the maximum steepness found from the non-linear simulation. The overall decaying trends and many of the maximum and minimum peaks are perceived in the plots from the non-linear model and ray tracing. The peaks in figures 3.3(a) and 3.4(a) correspond to the locations where the

short wave refracted against a phase of the inertia wave. In figures 3.3(b) and 3.4(b) the peaks coincide with the regions where the highlighted green rays from figures 3.1(c) and 3.2(b) refract with the inertia wave. The valleys in figures 3.3(a)-3.3(b) and 3.4(a)-3.4(b) result from the propagation of the short wave or the ray through a region of strong shear until the next inertia wave phase is encountered. Note that the final steepness after the short wave leaves the encounter is different in the non-linear and linear models. These differences between the two results are attributed to the comparison of a finite wave packet to a single ray.

Notice that for the steepness plots of third and first kind encounters, figures 3.3(a)-3.3(b) and 3.4(a)-3.4(b), the strong refractions occur at earlier times during the interactions. These strong refractions are the factors that most likely result on instabilities leading to overturning and wave breaking. The locations of strong refractions depend on the size of the envelope of the inertia wave. In this study the size of the envelope of the inertia wave is only big enough to contain one full wavelength of the inertia wave. Thus, any simulations performed in this model with an inertia wave envelope less than L=35 m are invalid since the resultant wave packet is smaller than an inertia wave.

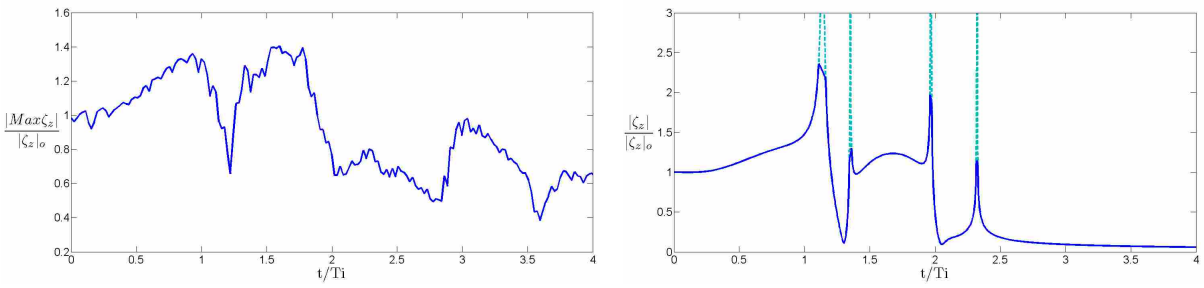

(a) (b)

Figure 3.3: Figure 3.3(a) shows the maximum steepness at each time step normalized by the initial steepness. Figure 3.3(b) is the normalized steepness of the short wave through time, obtained from the highlighted ray seen in Figure 3.1(c)

3.2 Parameterization of instabilities

Using the information obtained from the steepness, the shear exerted by the large inertia wave and the critical criteria for wave stability $(1/4)$, the gradient Richardson number is separated

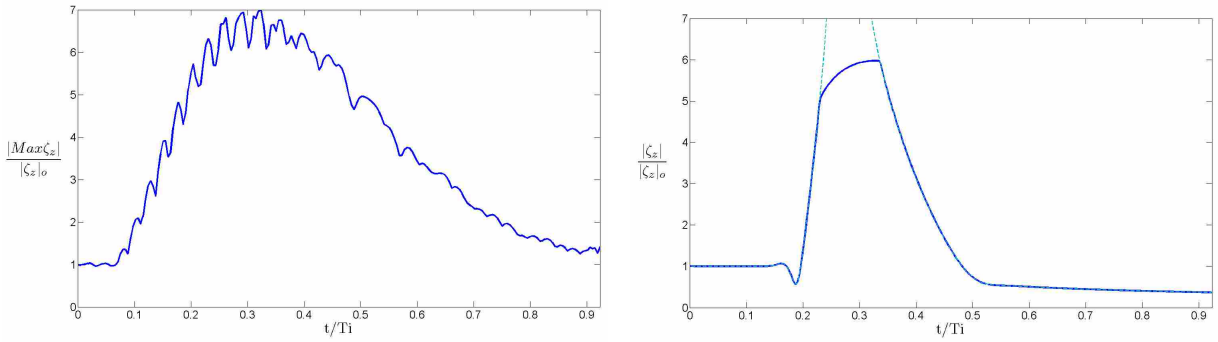

(a) (b)

Figure 3.4: Steepness plots corresponding to the encounters shown in figures 3.2(a) and 3.2(b). Figure 3.4(a) is the steepness calculated with the non-linear model. Figure 3.4(b) is the steepness found using the linear model.

into an angle as explained in the methods section of this thesis (See also Winters [1]),

$$\theta = \tan^{-1}\left[\frac{\frac{1}{4}\left(\frac{\mathrm{dU}}{\mathrm{dz}}\right)^2}{N^2\left(1-\frac{\partial\zeta}{\partial z}\right)}\right]. \tag{3.1}$$

The angle (θ) will fall into one of three stability regions: stable, shear unstable, or purely convectively unstable. In the instability chart, figures 3.5 and refnum instability chart 3rd knd enc, the dashed line corresponds to an angle $\theta = 45^\circ$ which is the boundary that separates the stable (below) and shear unstable (above) regions. The solid line corresponds to an angle $\theta = 90^\circ$ which is the borderline that differentiates between shear instabilities (below) and purely convective instabilities (above). Since the short wave steepness (ζ_{z0}) and the inertia wave shear (dU/dz) are time dependent, the angle θ is calculated at each time step and the results are plotted in the instability chart (figure 3.5) represented by crosses for the 2d non-linear results and open circles for the linear results. The instability chart corresponding to a first kind encounter is represented in figure 3.6. The crosses are the instabilities calculated using the non-linear model and the circles are the instabilities found from ray tracing. Notice that the instabilities captured for first kind encounters have a time-span which is much longer than instabilities found in figure 3.5.

In the non-linear simulation a small initial steepness, $\zeta_{z0} = 0.01$, was chosen so the model was stable throughout the interaction. However such a small initial steepness does not produce any convective instabilities. Assuming the temporal changes in the steepness are similar for other

initial steepnesses, although dynamics may change with increasing steepness, one can multiply the ratio of maximum steepness by a value that will assure convective instabilities (i.e. 0.8). Therefore, the original maximum steepness ratio is multiplied by a factor of 0.8 shifting the ratio upwards and reaching values greater than unity at some inertial periods. When the maximum steepness ratio is greater than unity convective instabilities are captured and noted, by the crosses in figure 3.5, between inertia periods $t/T_i = 0.6$ to 1.75 and in figure 3.6, between inertia periods $t/Ti = 0.1$ to 0.9. The initial steepness in ray tracing is initialized to 0.8 matching the initial steepness in the non-linear model. As a result the steepness from ray tracing reaches values greater than unity between inertia periods $t/T_i = 0.6$ to 1.75 in third kind encounters, depicted in figure 3.5 with the open circles and between inertia periods $t/Ti = 0.1$ to 1, depicted with the open circles in figure 3.6. Note that the same basic instabilities are expected from both models.

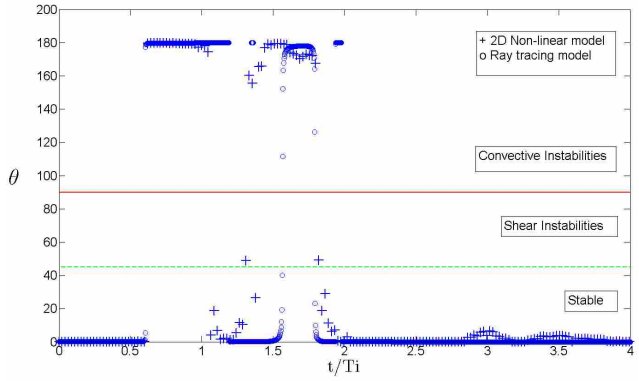

Figure 3.5: This is an instability chart separated into a convective instability ($\theta > 90°$), shear instability ($\theta > 45°$) and stable region ($\theta < 45°$). For this particular encounter convective instabilities are captured between inertia periods 0.6 to 1.75 in both models. The convective instabilities for the 2d non-linear and linear models are signaled by the crosses and open circles respectively. Note, that the inertia periods when the instabilities occur correspond to the inertia periods when the steepness ratio was greater than unity.

3.3 Instability timescales

Sutherland [17] proposed that a second instability condition was required for waves to overturn and break; that the timescale of the convective instability is larger than the period of the short wave. Looking at the instability chart, one can track how long instabilities will last by knowing

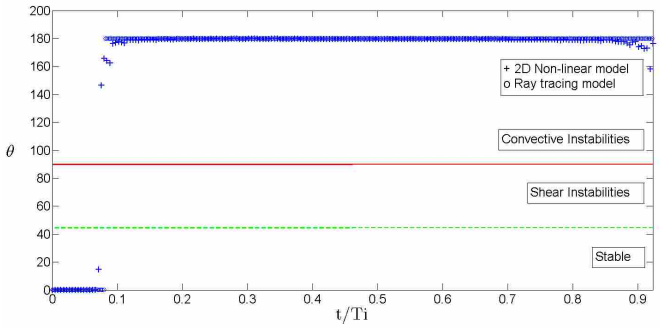

Figure 3.6: This is an instability chart for an encounter when the short wave approaches with a fast group speed. Convective instabilities are captured after inertia period 0.08 in both models. The convective instabilities for the 2d non-linear and linear models are signaled by the crosses and open circles respectively.

the beginning and ending inertia periods ($\Delta t/T_i$) of the instability. The timescale of the instability is superimposed on the local timescale of the short wave ($T = 2\pi/\omega$) in figures 3.7 and 3.8. The instability threshold (figures 3.7 and 3.8) includes open circles, for the timescales of the instabilities found in ray tracing, and crosses, for the timescales found in the 2d fully non-linear model. The solid and dashed lines in these plots represent the timescale of the short wave calculated from the non-linear and ray tracing simulations respectively. In figure 3.7 the timescale of the instability is much larger than the timescale of the short wave between inertia periods of approximately 0.6 to 1.75 corresponding to the convective instabilities depicted in figure 3.5. In the same manner in figure 3.8 the timescale of the instability is much larger than the timescale of the short wave between inertia periods 0.1 to 1 corresponding to the convective instabilities depicted in figure 3.6. Hence in theory instabilities had enough time to grow and develop into breaking waves. Note the difference in scales between the instabilities from the non-linear model and the instabilities found in the ray tracing model. In most encounters the ray tracing overestimates or underestimates the timescales of the instabilities. This is observed because the Airy function approximations may overestimate and in some instances underestimate the magnitude of the amplitude at the caustics. Recall that the steepness is proportional to the amplitude. Thus, the deviations of the amplitude are carried over to the steepness resulting in overestimates and/or underestimates of the instability timescales.

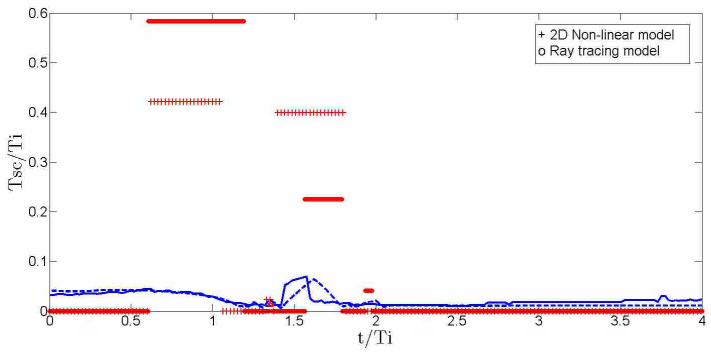

Figure 3.7: Instability threshold calculated from the instability results found in figure 3.5 from both models. The y axis denotes the magnitude of the timescale normalized by the period of the inertia wave. Comparing the magnitude of the normalized timescale of the instabilities (red), to the timescales of the short waves (blue) one notices that at some time periods the timescale of the instability is much larger. Hence the short wave is expected to overturn and break.

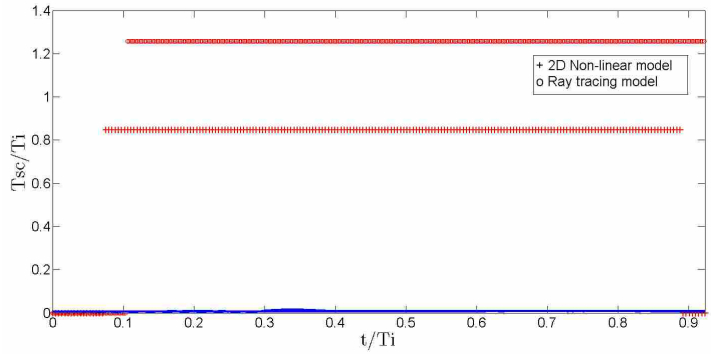

Figure 3.8: Instability threshold calculated from the instability results found in figure 3.5 from both models. The y axis denotes the magnitude of the timescale normalized by the period of the inertia wave. Comparing the magnitude of the normalized timescale of the instabilities (red), to the timescales of the short waves (blue) one notices that at some time periods the timescale of the instability is much larger. Hence the short wave is expected to overturn and break.

3.3.1 Instability timescale dependence on initial short wave steepness

The instabilities captured and their respective timescales are highly dependent on the initial steepness of the short wave. Figure 3.9 presents a particular example of a short wave approaching with a group speed much faster than the phase speed of the inertia wave (first kind encounter). This plot shows the changes of the steepness in time normalized by the initial steepness of the short wave. Notice the two cusps that occur at inertia periods 0.2 and 1.3. These cusps signal

the locations in time where the short wave refracts with one of the phases of the inertia wave. In the first cusp the steepness increases drastically ($\zeta_z = 10\zeta_{z0}$) and the large steepness persist and increases reaching a maximum at inertia period 0.7. Afterwards the steepness decreases slightly until the next refraction is observed at inertia period 1.3. Recall that the steepness is normalized by the initial steepness, hence the value of the initial steepness will determine whether or not instabilities will be present. Notice in figure 3.9 the three lines, one dashed, one dotted and one solid. Each line has its associated initial steepness on the right hand side of the plot and the lines represent the steepness ratio necessary for instability ($\zeta_z > 1$) to occur. For an initial steepness of 0.07 a change in the steepness ratio from 1 to the maximum steepness ever reached is not large enough for convective instabilities to develop. In contrast for initial steepness 0.09 a change in the steepness ratio from 1 to the maximum steepness ever reached results in a convective instability, which lasts about 1/4 of an inertia period. An initial steepness of 0.1 and a change in the steepness ratio from 1 to the maximum steepness ever reached yields a convective instability with a timescale long enough to estimate breaking. Although this example is particular to the interaction shown, all first kind encounters behave very similar.

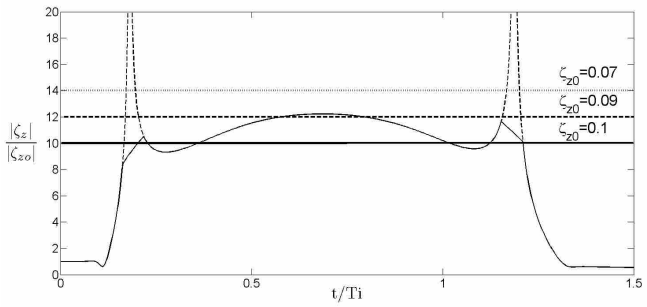

Figure 3.9: Steepness change for a short wave approaching at fast group speeds. When the initial steepness is very small, the steepness is never greater than unity. As the initial steepness increases the steepness grows past unity and in some instances it remains greater than unity for prolong times.

For third kind encounters (short wave approaching with a group speed slower than the phase speed of the inertia wave) the changes in the steepness are different than in first kind encounters. In most third kind interactions the steepness, as shown in figure 3.10, does not change drastically

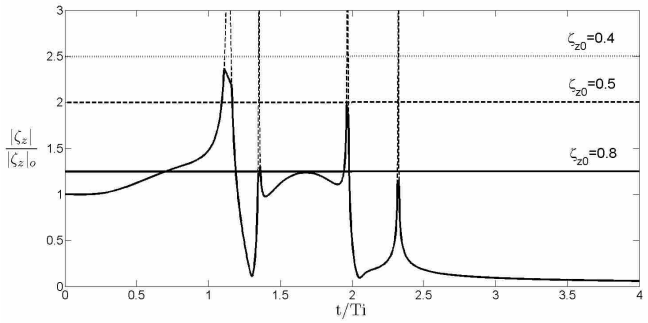

Figure 3.10: Steepness change for a short wave approaching at slow group speeds. When the initial steepness is very small, the steepness is never greater than unity. As the initial steepness increases the steepness grows past unity and in some instances it remains greater than unity for prolong times.

as observed in first kind encounters (See figure 3.9). In some instances the steepness increases enough to result in convective instabilities, but the associated timescale is not long enough to assume breaking may occur. In the same manner as in first kind encounters, the instabilities and timescales depend on the initial steepness of the short wave in third kind encounters. Although the following analysis is for this specific third kind encounter, most third kind interactions display very similar steepness changes. If the short wave propagates with an initial steepness of 0.4 a change in the steepness ratio from 1 to the maximum steepness ever reached is not sufficient for convective instabilities to develop. For an initial steepness 0.5 a change in the steepness ratio from 1 to the maximum steepness ever reached results in a convective instability, which lasts about 1/3 of an inertia period. An initial steepness of 0.8 and a change in the steepness ratio from 1 to the maximum steepness ever reached yields a convective instability with a timescale long enough to estimate breaking. Therefore as stated earlier, the outcome of the instability and its timescale is directly related to the initial steepness of the short wave.

3.4 Wave breaking estimates

3.4.1 Cut off and shifting factors

The stability analysis performed up to this point is comparing the refraction and steepness changes of a single ray which is suppose to represent a short wave packet. To find a more accu-

rate representation in the linear model of a short wave packet refracting, the following procedure is followed. The results from the stability analysis performed in the non-linear simulations and ray theory are contrasted to quantify the accuracy and precision of the linear approximations and amplitude calculations relative to the non-linear model. The comparison is based on the steepness parameter and the locations in time where the refractions match. The test is performed for a spectrum of short waves spaced equally by the ratio (c_{gz}/C) initialized at random z locations and moving with group speeds slower, equal and greater than the phase speed of the inertia wave corresponding to third, second and first kind encounters respectively. The maximum steepness ratio calculated from the non-linear model (i.e figure 3.3(a)) is matched to the refractions observed in the corresponding perturbation density plots (i.e figure 3.1(b)). The comparison indicates what part of the wave packet is being represented by the normalized steepness and how the steepness changes in relation to the refractions. This information is used to specify, in the linear model, the rays and their steepnesses at caustic regions that will be used for comparison with the non-linear results. To support the selection of the particular group of rays in the linear model, the refractions corresponding to the isolated rays are matched to the perturbation density from the numerical simulations and an average of the steepnesses of the isolated rays is calculated. Once the steepnesses are averaged, a single magnitude from ray tracing is compared to a single magnitude from the non-linear model.

When the short wave packet split and refractions occurred at different phases of the inertia wave as in figure 3.11(a), it was noticed that the steepness in the non-linear model always revealed large changes corresponding to the strong refractions occurring in the first phase (see figure 3.11(b)). This phenomenon was taking place because the maximum steepness throughout the entire vertical domain was computed for each time-step. Consequently, stronger refractions dominate the result of the maximum steepness at each time-step. Additionally, for short waves approaching with a group speed faster than the phase speed of the inertia wave (figure 3.12(a)) it was found that most of the short wave packet weakly refracted and continued propagating vertically. The resulting normalized maximum steepness (figure 3.12(b)) associated with these fast short waves reveals large changes in its steepness magnitude, around the inertia period, when the short wave interacts with the inertia wave. Afterwards, the steepness decays to a value close to the initial steepness ratio. To match either of these cases in ray tracing, the same procedure as

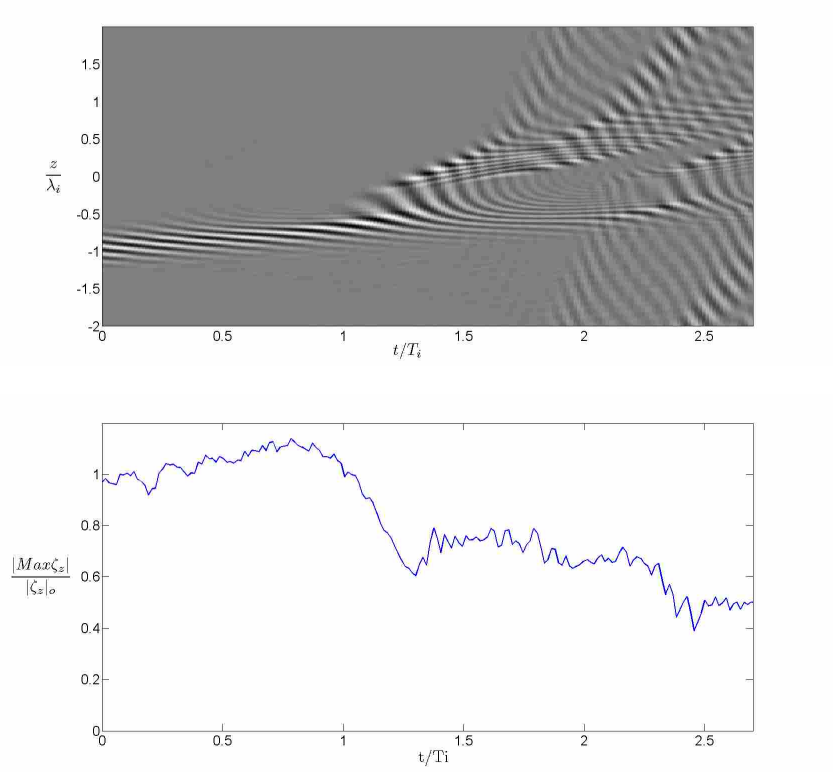

Figure 3.11: Figure 3.11(a) is a short wave approaching the inertia wave with a slow group speed. The short wave refracts in more than one phase of the inertia wave. Figure 3.11(b) is the corresponding normalized steepness, which displays large changes matching with the inertia period of the first refraction.

explained above is followed. A graphical representation of the comparison procedure is displayed in figure 3.13(a) and 3.13(b).

Table 3.1: Summary of runs conducted to find cutoff and adjustment values. The heading on the last column A_r/A_n is the average ratio of ray steepness calculations over non-linear steepness calculations.

Interaction type	Number of runs	c_{gz0}/C Hi	c_{gz0}/C Low	Steepness range	A_r/A_n
1st kind (1)	11	6	1.2	4.49-2.01	0.68
1st kind (2)	11	12	6	6.1-3.32	0.61
1st kind (3)	9	16	12	5.4-3.25	1.62
2nd kind	12	1.2	0.6	3.1-1.93	0.70
3rd kind	9	0.6	0.16	1.74-0.75	1.10

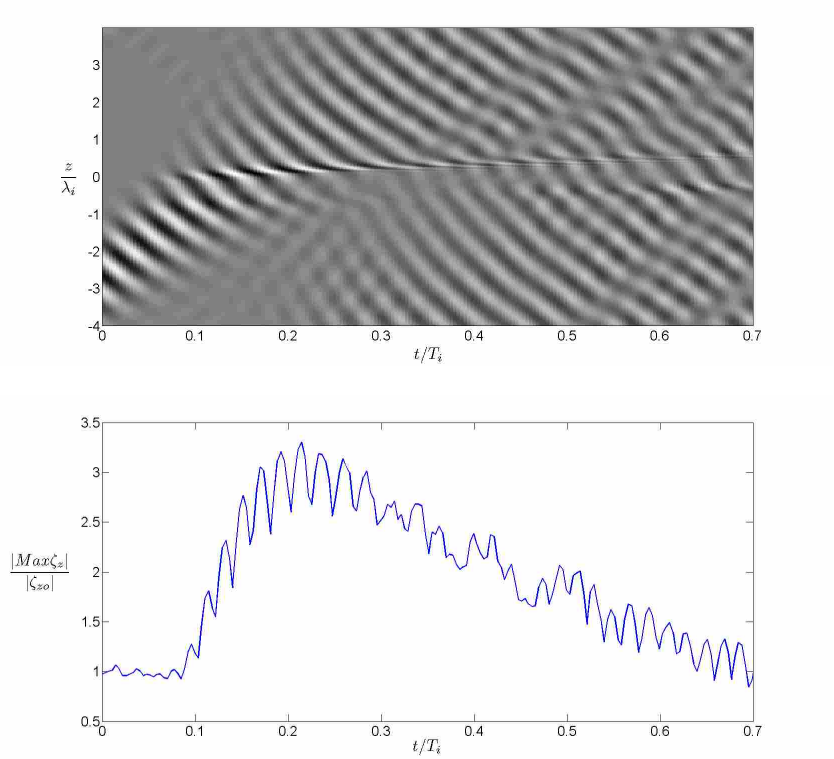

Figure 3.12: Figure 3.12(a) is the density perturbation field revealing a short wave approaching an inertia wave with a fast group speed. The short wave is not refracted strongly, but instead most of it continues propagating upwards pass the inertia wave. Figure 3.12(b) is the normalized steepness corresponding to the encounter shown in figure 3.12(a).

The results of the comparisons are outlined in table 3.1. These comparisons are used to find cutoff and shifting values for the steepnesses from ray theory that are much larger than the ones found in the non-linear model. The cutoff will cap the ray tracing steepness estimates. The cutoff is taken from the largest value of the steepness found in the steepness ranges calculated in the non-linear model individually for first, second and third kind encounters. These ranges are displayed in the fifth column of table 3.1. The shifting factor, used after the steepnesses are cut off, is utilized to correct common under predictions or over predictions noted between ray tracing and the numerical simulations. The shifting factor will match the ray tracing steepness results to the more accurate numerical simulations. These shifting factors are found in the last column of table 3.1. In some instances after the shifting factor is employed, the steepness may increase beyond the cutoff value for a particular interaction. In such cases the cutoff value is used once again. The first kind encounters (short waves approaching rapidly) are grouped into three sub-

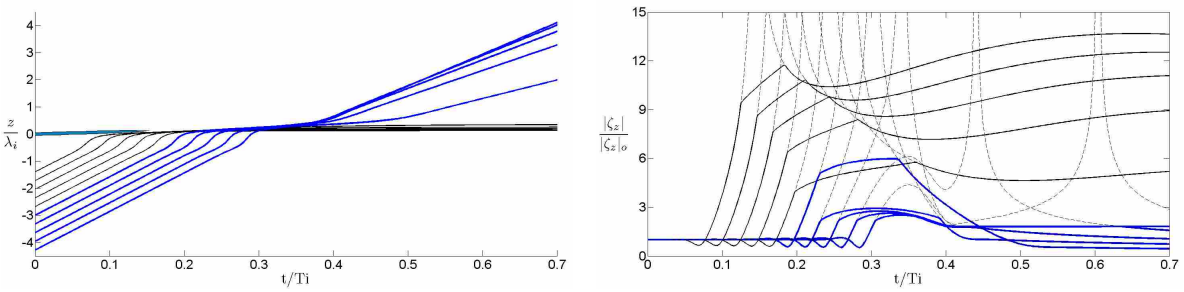

Figure 3.13: Figure 3.13(a) shows a short wave approaching an inertia wave faster than the phases of the inertia wave. The bold rays are selected because they simulate the non-linear behavior very close. The steepnesses of these rays are presented in figure 3.13(b) with bold lines to easily relate them to the ray tracing. The average of these bold steepness lines is taken and the resulting value is used for comparison against the normalized steepness from the non-linear model. The dashed lines in figure 3.13(b) show the steepness values before the Airy function is used to approximate singularities.

segments, each delimited by an upper and lower velocity ratio c_{gz0}/C. Each sub-segment has a corresponding steepness range and the maximum value of the steepness range is used as the cutoff to cap steepnesses found in the ray tracing model. These ranges are selected because they are common results of all the simulations performed. A ratio of the steepness found from both models ($\zeta_{z,r}/\zeta_{z,n}$), at regions of strong refraction, is calculated for each segment and these factors are used to shift the steepnesses. For second kind encounters (short waves approaching at the phase speed of the inertia wave) and third kind encounters (short waves approaching slowly), the exact same procedure is followed.

3.4.2 Instability maps

Instability maps for a range of initial short waves and inertia wave conditions are created in ray tracing. These maps use the timescale estimates previously discussed to display the waves with instabilities and time-scales conducive to wave breaking. Figures 3.14(a) and 3.14(c) present the instability maps before the cutoff and shifting factors are employed. Each of these maps show multiple simulations represented by each of the squares in the plot. To randomize the results in the maps, the short waves entered the inertia waves at different phases. The idea of this instability map is to encompass a wide spectrum of encounters that may be seen in observations and have

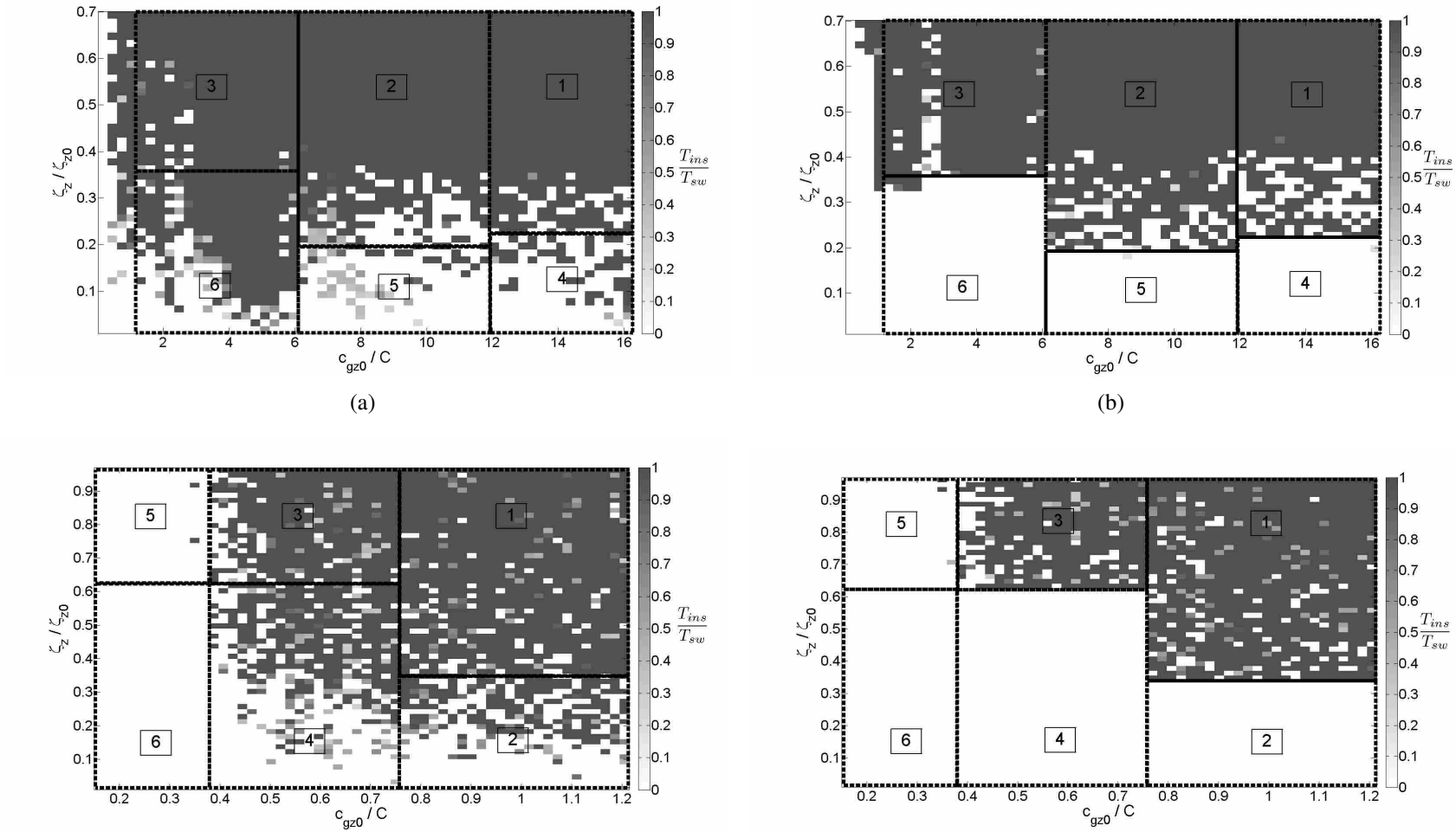

Figure 3.14: Instability maps for 1st, 2nd and 3rd kind encounters. Figures 3.14(a) and 3.14(c) are maps without any adjustments or cutoffs. Figures 3.14(b) and 3.14(d) are maps with adjusted steepness values using the cutoffs and ratios presented in table 3.1.

a general idea of the waves that may overturn and break when they interact with common inertia waves. The vertical domain for the contour maps of first kind encounters in figures 3.14(a) and 3.14(b) is limited to a maximum of $\zeta_z/\zeta_{z0} = 0.7$. This is because at a steepness ratio greater than 0.7 all simulated waves for first kind encounters refracted to a steepness greater than one for longer than the timescale of the short wave and are estimated to break regardless of initial group speed.

The contour maps depend on the approximations of the steepness found from the linear model, which is not as accurate as the non-linear model. Therefore, the comparison analysis summarized in table 3.1 is used to plot more accurate instability maps. The resulting contour maps are displayed in figures 3.14(b) and 3.14(d).

Notice in figure 3.14(a) that all the short waves approach the inertia wave with fast group speeds and it seems that regardless of the initial magnitude of the steepness the waves are very likely to break. In contrast in figure 3.14(c) all the short waves approach the inertia wave slowly and with small initial steepness, resulting in short waves that are less likely to break. When the short waves start with an initial steepness greater than approximately 0.3 and a group speed 6 times or greater than the phase speed of the inertia wave, the likelihood of these waves breaking is extremely large. This occurs because waves with larger group speeds exhibit instabilities that begin at locations of strong refraction and persist through the regions where the strongest shear is located (between strong refractions).

These figures are divided into regions to better estimate the percentage of waves expected to break as a function of the initial wave-field. A ratio of the number of encounters with timescales ($T_{ins}/T_{sw} > 1$) over the total number of encounters within each region is used to estimate the breaking percentages. Table 3.2 shows the corresponding divisions of the contour maps and their respective percentages of waves estimated to break. The percentage breaking is zero for all steepness values below the lower steepness limits in table 3.2. The percentage breaking is one hundred for all steepness values above the upper steepness limits in table 3.2.

Notice regions (4, 5 and 6) in figures 3.14(a) and 3.14(b) and regions (2, 4 and 6) in figures 3.14(c) and 3.14(d). These regions changed drastically after the adjustments displayed in table 3.1 were implemented. The results of the simulations from the linear model shown in figures 3.14(a) and 3.14(c), severely overestimated the maximum steepnesses of a large number of short waves, which yielded a larger estimate of waves breaking. After the cutoff and shifting factors

Table 3.2: Percentage of waves expected to break without adjustments and with adjustments found in the comparison of both models.

Interaction type	c_{gz0}/C range	Steepness range	Breaking % with adjustment	Breaking % without adjustment
1st kind (1)	12-16	0.19-0.7	92.37	92.56
1st kind (2)	6-12	0.17-0.7	89.57	87.59
1st kind (3)	1.2-6	0.36-0.7	94.26	96.84
1st kind (4)	12-16	0.01-0.19	21.03	0
1st kind (5)	6-12	0.01-0.17	5	0
1st kind (6)	1.2-6	0.01-0.36	60.05	4.66
2nd kind (1)	0.75-1.2	0.35-0.98	84.03	85.62
2nd kind (2)	0.75-1.2	0.01-0.35	30.8	0
3rd kind (3)	0.37-0.75	0.63-0.98	72.88	73.5
3rd kind (4)	0.37-0.75	0.01-0.63	34.35	0
3rd kind (5)	0.16-0.37	0.63-0.98	0.7	0.7
3rd kind (6)	0.16-0.37	0.01-0.63	0	0

were applied to the maximum steepnesses, an improved and validated estimate of wave breaking was obtained (see figures 3.14(b) and 3.14(d)).

It is necessary to clarify that the results obtained in table 3.2 are approximations of the percentages of wave breaking before and after the adjustments were made. These percentages are found on two contour maps which are a little different. The contour map without the adjustments is generated first and the map with the adjustments is developed. The two maps are not identical because each interaction modeled has a random location in depth where the short wave starts. Hence, the two maps differ in the locations where short waves start for each simulation.

CHAPTER 4. SUMMARY AND CONCLUSION

4.1 Summary

Linear and 2d non-linear models were utilized to study the dynamics of an interaction between a short internal wave and an inertia wave. Specifically, the effect of the interactions on the stability and breaking of short waves was analyzed. The linear model was a good alternative to the more computationally demanding 2d non-linear model. However, ray tracing (linear model) fails at regions of strong refraction and singularities are present in the calculation of wave steepness. These steepnesses were approximated using the Airy function, a procedure explained thoroughly in the methods section. The 2d non-linear model was utilized to simulate the same wave interactions and corresponding values for the steepness were calculated. These steepnesses values were compared to the linear approximations to understand how well the Airy function estimated the steepness for the singularities.

A stability analysis was carried out as the second major step in this research. The steepness calculations from the linear and non-linear models in addition to the shear from the inertia wave were used together to form the gradient Richardson number. This expression was used to parameterize the relative influence of convective and shear instabilities during interactions. Since steepness and shear are both functions of time, the instabilities were displayed through time. The instability timescales were part of the stability analysis. Hence, the timescale of the instability was contrasted to the scale of the short wave. The linear model was used to simulate interactions from a spectrum of short waves and a fixed inertia wave. Each of the short waves in the spectrum was given an initial steepness and group speed to find a relationship between instabilities and inertia wave characteristics. A map was developed displaying the approximate number of waves estimated to break from the initial spectrum of waves using ray tracing. Since these maps depended on the accuracy of the approximations from the linear model, a statistical analysis was performed to find

average cut-off and shifting factors to the steepness approximations. These cut-off and shifting factors were applied to the instability maps resulting in an improved estimate of wave breaking.

4.2 Conclusions

The first objective of this research was to validate the Airy function approximations to the short wave amplitudes by comparing the results to the 2d non-linear model. This objective was accomplished by comparing the linear model to the non-linear model to have a better understanding of how well the Airy function approximates the amplitudes. It was found that in general the Airy function diverged the most when approximating first kind encounters with group speeds greater than 12 times the phase speed of the inertia wave (C) and also when approximating third kind encounters. For all other encounters the approximations deviated on average by 66%.

The maximum amplitude approximations found using the Airy function were compared to the maximum amplitude calculated in the non-linear model. The comparison showed that the Airy function approximations were deficient for wave interactions with group speeds greater than $12C$. For these interactions the average difference in the results was 162%. The Airy approximations also lack accuracy when estimating the amplitude of third kind encounters ($c_g < C$). For these type of interactions the average difference in the results was 110%. The estimates of the amplitude for second kind encounters and first kind encounters with group speeds less than $12C$ show an average deviation of 66%. The estimates of the accuracy of the Airy function are an important contribution for engineers, mathematicians and scientist who may use the Airy function to approximate the results of another solution as it was used in this study.

The second objective was to perform a stability analysis and define instabilities using the steepness and the inertia wave shear parameters. During the stability analysis and after performing multiple simulations it was identified that convective instabilities had the largest influence on short wave instability and when shear instabilities were present, their influence was very small. This is because the strength of the shear from the inertia wave is very small relative to the strength of overturned density gradients. Regardless of the strength of the shear, a forcing momentum in the form of shear was present which increased the wave steepness, in some instances, by ten times or more. These large changes in the wave steepness were definitely conducive to isopycnal overturning and convective instabilities.

In the stability analysis, the temporal dependence of the instabilities was also accounted for. To do this, the timescales of the instabilities were contrasted with the timescales of the short waves. It was determined that in some cases instabilities were present, but their associated timescale was not longer than the timescales of the short wave so they would not overturn. In these cases short waves developed instabilities after the first interaction with the inertia wave. Then the unstable short waves continued to propagate for a very short time until a second interaction occurred. In this instance, when the second interaction was reached the amplitude of the wave decreased, eliminating the instabilities and allowing the wave to continue to propagate.

From the stability analysis it was noticed that instabilities behave according to the initial steepness and group speed of the short wave. It was found for first kind encounters, that the likelihood of meeting the theoretical conditions for wave breaking was high. This occurs because the initial steepness of the wave changes significantly and it was sustained for long periods of time. In general, the faster the short wave was approaching the inertia wave the larger the change in the steepness magnitude observed, and the wave was more likely to become unstable.

The initial steepness also had a significant influence on the outcome of the instabilities, as expected. Larger initial steepness magnitudes required smaller changes in wave properties for the wave to cross the stability threshold, overturn and develop convective instabilities. The overall behavior of the interactions showed that the percentage of waves estimated to break was the highest when the group speed and initial steepness magnitudes were the largest. For encounters of waves approaching slowly, it was found that below a group speed of about 0.37 C the estimated wave breaking was zero regardless of the initial steepness magnitude. Thus, at these group speeds the refractions were not strong enough to amplify the steepness for convective instabilities to appear.

The third objective was to use the linear model to develop a map that demonstrates estimates of wave breaking as a function of initial wave properties. A contour map was created showing the breaking estimates for a large spectrum of short waves. These maps are shown in figures 3.14(a) through 3.14(d). The darkest squares in this plot show wave-wave interactions which developed convective instabilities that persisted long enough to estimate wave breaking. The white squares correspond to interactions with not instabilities and any other gray shade are those encounters with instabilities that do not have a timescale long enough to estimate breaking. These contour maps are a significant contribution to the field of internal waves because the chart can provide a

general idea of the percentage of waves estimated to break from an field of waves observed in the ocean. It is important to mention that the length-scale of the inertia wave envelope in these simulations is only big enough to capture one full wavelength of the inertia wave. Therefore if a smaller envelope is surrounding the inertia wave packet this model is no longer valid, because a smaller inertia wave envelope length-scale could not capture a full wavelength of the inertia wave.

First kind encounters show large changes in the steepness leading to convective instabilities. In addition a significant number of simulations show that the large steepness persisted for a long time with respect to the frequency of the short wave. First kind encounters with group speeds between 1.2 to 6 C display an estimated percentage breaking of 96%. First kind encounters with group speeds between 6 to 12 C show wave breaking percentage estimates of 87%. First kind encounters with group speeds between 12 to 16 C show a percentage of wave estimated to break of 92%. For second kind encounters it was found from the stability analysis that the steepness changes develop convective instabilities but only 85% of those meet the timescale requirement to estimate breaking. Third kind encounters with group speeds faster than 0.37 C display convective instabilities with only 73% of the interactions displaying a long enough timescale to estimate breaking. For both of these type of interactions the steepness changed less drastically than in first kind encounters and the larger magnitude of the steepness was not always sustained for a time period longer than the frequency of the short wave.

The bottom regions (4, 5 and 6) in figures 3.14(a) and 3.14(b) and regions (2, 4 and 6) in figures 3.14(c) and 3.14(d) demonstrate the largest changes in the estimates of wave breaking after the cut off and shifting factors are employed. For first kind encounters region (4) the percentage breaking changed from 21% to 0 %, first kind encounters region (5) shows a change from 5% to 0% and first kind encounters region (6) displays a change from 60% to 4%. Second kind encounters region (2) shows a percentage change from 30% to 0%. Third kind encounters region (4) has a change in the percentage of waves estimated to break from 34% to 0%

These large changes in the breaking percentage estimates take place because the approximations to the steepness in the linear model generally over predict the maximum magnitude of the steepness, which results in more short waves developing convective instabilities with large enough timescales to estimate breaking. Thus, the cutoff and shifting factors decrease the severity of the overestimates found from the linear model.

4.3 Future work

The effects of possible wave overturning on the interaction dynamics of short waves with inertia waves, due to the time dependence of the inertia wave, has been analyzed. Nevertheless, further studies are required to estimate the strength of internal wave breaking.

In addition further study of the regions boxed in the instability maps is necessary. A better understanding of the physics involved with the interactions is needed to explain the boundaries that exist between breaking and non-breaking estimates. This study would be better performed using a 3d non-linear model.

Lastly, it is recommended to use a 3d non-linear model to find the validity of our wave breaking estimates. The 3d non-linear model will be able to capture the characteristics of the breaking and the short waves that will actually break due to the interaction. The results of the 3d non-linear model can be used to further adjust the estimates of the linear model performed in this study. This is recommended because ray tracing is the most versatile and quick model for applications where multiple short waves interacting with inertia waves need to be modeled and estimates of breaking are of interest, such as in oceanic observations of fields of internal waves.

REFERENCES

[1] Winters, K. B., and D'Asaro, E. A., 1989. "Two-Dimensional Instability of Finite Amplitude Internal Gravity Wave Packets Near a Critical Level." *Journal of Geophysical Research,* **94**, pp. 12709–12719. viii, 5, 7, 10, 26, 27, 35

[2] Liu, W., Bretherton, F. P., Liu, Z., Smith, L., Rutland, C. J., and Rutland, H. L., 2010. "Breaking of Progressive Internal Gravity Waves: Convective Instability and Shear Instability." *Journal of Physical Oceanography,* **40**, pp. 2243–2263. viii, 8, 9, 16, 26

[3] Broutman, D., 1986. "On internal wave caustics." *Journal of Physics and Oceanography,* **16**, pp. 1625–1635. viii, 21, 22

[4] Garrett, C., 2003. "Mixing with latitude." *Nature Publishing Group,* **422**, p. 477. 2

[5] Egbert, G. D., and Ray, R., 2001. "Estimates of M2 tidal energy dissipation from TOPEX/Poseidon altimeter data." *Journal of Geophysical Research,* **106**, pp. 22475–22502. 2

[6] Munk, W., and Wunsch, C., 1998. "Abyssal recipies II: Energetics of tidal and wind mixing." *Deep-Sea Res.,* **45**, pp. 1977–2011. 2

[7] Simmons, H., Jayne, S., Laurent, L. W., and Weaver, A., 2004. "Tidally driven mixing in a numerical model of the ocean general circulation." *Ocean Modelling,* **6**, pp. 245–263. 3

[8] Bretherton, F. P., 1966. "The propagation of groups of internal gravity waves in a shear flow." *Journal of Roy. Meteorological society,* **92**, pp. 466–480. 5

[9] Broutman, D., and Young, W. R., 1986. "On the interaction of small-scale oceanic internal waves with near-inertial waves." *Journal of Fluid Mechanics,* **166**, pp. 341–358. 6

[10] Vanderhoff, J. C., Nomura, K. K., Rottman, J. W., and Macaskill, C., 2008. "Doppler spread of internal gravity waves by an inertia-wave packet." *Journal of Geophysical Research,* **113**, p. C05018. 6, 17, 31

[11] Bruhwiler, D. L., and Kaper, T. J., 1995. "Wavenumber transport: scattering of small-scale internal waves by large-scale wavepackets." *Journal of Fluid Mechanics,* **289**, pp. 379–405. 6

[12] Vanderhoff, J. C., Rottman, J. W., and Broutman, D., 2010. "The trapping and detrapping of short internal waves by an inertia wave ." *Physics of Fluids,* **22**, p. 126603. 6

[13] Sartelet, K. N., 2002. "Wave propagation inside an inertia wave. Part II: Wave breaking." *Journal of Atmospheric Sciences,* **60**, pp. 1448–1455. 6, 9

[14] Thorpe, S. A., 1999. "On the breaking of internal waves in the ocean." *Journal of Physical Oceanography,* **29**, pp. 2433–2441. 7

[15] Lombard, P. N., and Riley, J. J., 1996. "Instability and Breakdown of Internal Gravity Waves. I. Linear stability analysis." *Physics of Fluids,* **8**, pp. 3271–3288. 9, 26

[16] Pascale Lelong, M., and Dunkerton, T. J., 1998. "Inertia-Gravity wave breaking in three dimensions. Part II: convectively unstable waves." *Journal of the atmospheric sciences,* **55**, pp. 2489–2501. 10

[17] Sutherland, B. R., 2001. "Finite-amplitude internal wavepacket dispersion and breaking." *Journal of Fluid Mechanics,* **429**, pp. 343–380. 10, 27, 36

[18] Hayes, W. D., 1970. "Kinematic wave theory." *Proc.Roy.Soc.London,* **A320**, pp. 209–266. 19

[19] Peregrine, D. H., and Smith, R., 1979. "Nonlinear effects upon waves near caustics." *Phil.Trans.Roy.Soc.London,* **A292**, pp. 341–370. 21, 22

[20] Pedlosky, J., 2003. *Waves in the Ocean and Atmosphere*. New York: Springer. 25

[21] Desaubies, Y., and Smith, W. K., 1982. "Statistics of Richardson Number and Instability in Oceanic Internal Waves." *Journal of Physical Oceanography,* **12**, pp. 1245–1259. 26

[22] Grimshaw, R. H., 1977. "The modulation of an internal gravity-wave packet, and the resonance with the mean motion." *Studies of Applied Mathematics,* **56**, pp. 241–266. 28

[23] Broutman, D., Rottman, J. W., and Eckermann, S. D., 2004. "Ray methods for internal waves in the atmosphere and ocean." *Journal of Fluid Mechanics,* **36**, pp. 233–253. 31

APPENDIX A. WAVENUMBER DISPERSION

A.1 Wavenumber dispersion

The wavenumber dispersion occurs because a wave is enveloped with a Gaussian. The new wavepacket does not have a uniform wavelength as the original wave, instead it contains a collection of wavelengths that approximate the original wavelength. Therefore, the energy of a wavepacket is distributed among various wavenumbers ($2\pi/\lambda_i$, where λ_i is the wavelength). If the envelope length-scale chosen to make the wavepacket is short the spectrum of wavelengths representing the original wavelength is large and the energy will tend to spread among all wavelengths (wavenumbers). In contrary if the length-scale is long, the spectrum of wavelengths is smaller because a more uniform wavelength can be maintained inside the envelope. Hence, less energy is dispersed because there are less wavelengths (wavenumbers) to distribute it to. The effects of the length-scale of the envelope are observed in figures A.1(a) and A.2(a). Figure A.1(a) corresponds to an envelope length-scale of 14 m, compared to the envelope length-scale of figure A.2(a) which is 42 m. Notice the difference in dispersion which is more notorious for the envelope length-scale of 14 m. Also notice the initial wavenumber spectrum for the smaller envelope, figure A.1(b), originally has energy around the initial wavenumber $m_0 = 0.63$ but it is distributed in a broad bell curve around the vertical wavenumber (m_0), which means the energy is distributed among more wavenumbers with different vertical group speeds. The initial wavenumber spectrum for the larger envelope, figure A.2(b), originally has most of its energy accumulated very close to the initial wavenumber $m_0 = 0.63$ with less wavenumbers sharing the energy at different vertical group speeds.

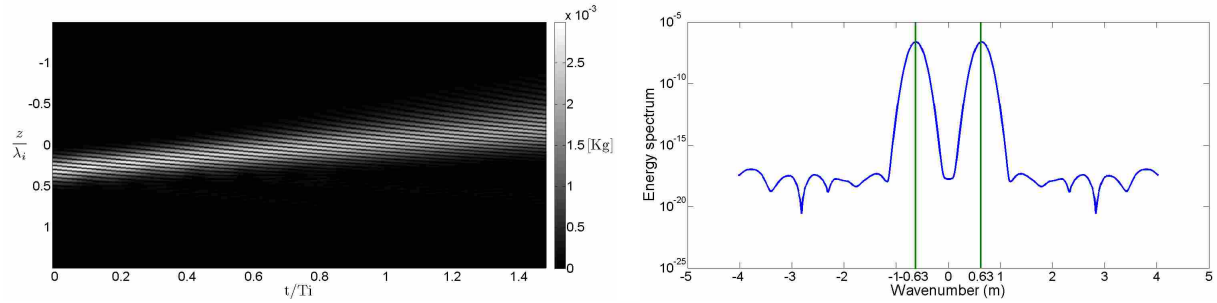

(a) (b)

Figure A.1: Figure A.1(a) is a freely propagating wave-packet with an envelope length-scale of 14 m. The small envelope length-scale of 14 m contains more wavelengths to approximate the original wave. Thus the energy is distributed among multiple wavenumbers. Figure A.1(b) is the wavenumber spectrum at the beginning of the simulation. This spectrum shows the energy concentrated around m=0.63 in a bell curve.

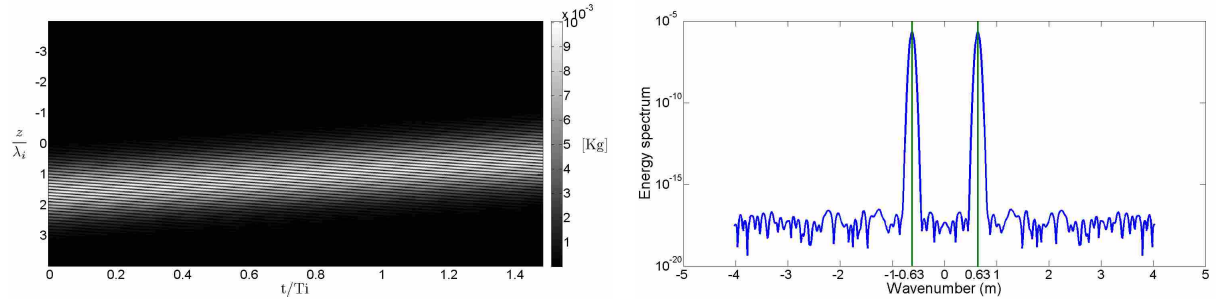

(a) (b)

Figure A.2: Figure A.2(a) is a freely propagating wave-packet with an envelope length-scale of 42 m. The larger envelope length-scale of 42 m diminishes the dispersion of energy. Figure A.2(b) is the wavenumber spectrum at the beginning of the simulation. This spectrum shows most of the energy concentrated at m=0.63 with a small amount of the energy at other wavenumbers.

APPENDIX B. POLARIZATION RELATIONS

The polarization relations, which define the perturbation density, pressure, and particle velocities, are determined from the linear Boussinesq equations, dispersion relation, and continuity.

A waveform solution to the partial differential equations shown in section 2.1 is assumed such

$$w' = w_0 \cos(\mathrm{kx} + \mathrm{ly} + \mathrm{mz} - \omega \mathrm{t}). \tag{B.1}$$

Take the relationship between ρ' and w'.

$$\frac{\partial \rho'}{\partial t} + w' \frac{d\bar{\rho}}{\mathrm{dz}} = \frac{\partial \rho'}{\partial t} + w_0 N^2 \cos(\mathrm{kx} + \mathrm{ly} + \mathrm{mz} - \omega \mathrm{t}) = 0, \tag{B.2}$$

$$\partial \rho' = -w_0 N^2 \frac{\rho_0}{g} \cos(\mathrm{kx} + \mathrm{ly} + \mathrm{mz} - \omega \mathrm{t}) \partial t. \tag{B.3}$$

Integrate both sides

$$\rho' = -\frac{w_0 N^2}{\omega} \frac{\rho_0}{g} \sin(\mathrm{kx} + \mathrm{ly} + \mathrm{mz} - \omega \mathrm{t}). \tag{B.4}$$

Follow the same procedure with the expression relating p' and w'.

$$\frac{1}{\rho_0} \frac{\partial p'}{\partial z} = -\frac{\partial w'}{\partial t} - \frac{\rho'}{\rho_0} g_z. \tag{B.5}$$

Substituting equations B.1 and B.4

$$\frac{\partial p'}{\partial z} = \rho_0 w_0 \omega \sin(\mathrm{kx} + \mathrm{ly} + \mathrm{mz} - \omega \mathrm{t}) + \frac{w_0 \rho_0 N^2}{\omega} \sin(\mathrm{kx} + \mathrm{ly} + \mathrm{mz} - \omega \mathrm{t}). \tag{B.6}$$

$$\partial p' = \rho_0 w_0 \sin(\mathrm{kx} + \mathrm{ly} + \mathrm{mz} - \omega \mathrm{t}) \left(\omega + \frac{N^2}{\omega} \right) \partial z. \tag{B.7}$$

Integrate both sides and replace w' and $N^2 = (\omega^2 k^2)/k_h^2$, where $k_h^2 = k^2 + l^2$

$$p' = \frac{w'\rho_0\omega}{m}\left(\frac{-m^2}{k^2+l^2}\right) = -w'\rho_0\omega\left(\frac{m}{k^2+l^2}\right). \tag{B.8}$$

Use the equations derived for ρ', p' and w' to solve for the particle velocities u' and v'.

$$\frac{\partial u'}{\partial t} = -\frac{1}{\rho_0}\frac{\partial p'}{\partial x}. \tag{B.9}$$

Substitute the partial derivative of equation B.8 with respect to x

$$\frac{\partial u'}{\partial t} = \frac{\omega m}{k^2+l^2}\frac{\partial w'}{\partial x}. \tag{B.10}$$

Plug $\partial w'/\partial x = w_0 k \sin(\mathrm{kx} + \mathrm{ly} + \mathrm{mz} - \omega \mathrm{t})$ and integrate both sides

$$u' = -\frac{mkw'}{k^2+l^2}. \tag{B.11}$$

$$\frac{\partial v'}{\partial t} = -\frac{1}{\rho_0}\frac{\partial p'}{\partial y}. \tag{B.12}$$

Plug the partial derivative of equation B.8 with respect to y

$$\frac{\partial v'}{\partial t} = \frac{\omega m}{k^2+l^2}\frac{\partial w'}{\partial y}. \tag{B.13}$$

Substitute $\partial w'/\partial y = w_0 l \sin(\mathrm{kx} + \mathrm{ly} + \mathrm{mz} - \omega \mathrm{t})$ and integrate both sides

$$v' = -\frac{mlw'}{k^2+l^2}. \tag{B.14}$$

APPENDIX C. DISPERSION RELATION

The partial derivative of the z momentum with respect to time is taken and the following equation is obtained:

$$\frac{\partial^2 w'}{\partial t^2} + N^2 w' = -\frac{1}{\rho_0}\frac{\partial^2 P'}{\partial t \partial z}. \tag{C.1}$$

Then the partial derivative of the x and y momentum is taken in the manner shown below.

$$\frac{\partial}{\partial x}\left(\frac{\partial u'}{\partial t}\right) = -\frac{1}{\rho_0}\frac{\partial^2 P'}{\partial x^2} \tag{C.2}$$

$$\frac{\partial}{\partial y}\left(\frac{\partial v'}{\partial t}\right) = -\frac{1}{\rho_0}\frac{\partial^2 P'}{\partial y^2}. \tag{C.3}$$

Adding these two equations results in the following expression:

$$\frac{\partial}{\partial t}\left(\frac{\partial u'}{\partial x} + \frac{\partial v'}{\partial y}\right) = -\frac{1}{\rho_0}{\nabla_H}^2 P', \tag{C.4}$$

where ∇_H^2 is $\partial^2/\partial x^2 + \partial^2/\partial y^2$. Applying the ∇_H^2 to equation C.1 gives:

$$\frac{\partial^2\left({\nabla_H}^2 w'\right)}{\partial t^2} + N^2 {\nabla_H}^2 w' = -\frac{1}{\rho_0}\frac{{\nabla_H}^2 P'}{\partial t \partial z}. \tag{C.5}$$

Notice that the term $-\nabla_H^2 P'/\rho_0$ is common in equations C.4 and C.5. Substituting equation C.4 into equation C.5 results in the following equation:

$$\frac{\partial^2\left({\nabla_H}^2 w'\right)}{\partial t^2} + N^2 {\nabla_H}^2 w' = \frac{1}{\partial t \partial z}\left[\frac{\partial}{\partial t}\left(\frac{\partial u'}{\partial x} + \frac{\partial v'}{\partial y}\right)\right]. \tag{C.6}$$

Using the continuity expression 2.5 in equation C.6 yields:

$$\frac{\partial^2\left(\nabla^2 w'\right)}{\partial t^2} + N^2 {\nabla_H}^2 w' = 0. \tag{C.7}$$

Assuming a wave form solution for this partial differential equation one can propose the following answer.

$$w' = w_0 cos(kx + ly + mz - \omega t). \tag{C.8}$$

One can substitute this solution into equation C.7 and solving for ω yields:

$$\omega^2 = \frac{N^2\left(k^2 + l^2\right)}{k^2 + l^2 + m^2}. \tag{C.9}$$

In the case of the inertia waves when the Coriolis force is significant, the dispersion relation becomes

$$\omega^2 = \frac{N^2\left(k^2 + l^2\right) + f^2 m^2}{k^2 + l^2 + m^2}. \tag{C.10}$$

APPENDIX D. RAY EQUATIONS

Starting with the waveform solution equation $w' = w_0 \cos(\mathrm{kx} + \mathrm{ly} + \mathrm{mz} - \omega \mathrm{t})$ and letting $(kx + ly + mz - \omega t) = -\alpha$ one can define the following expressions.

$$\omega = \frac{\partial \alpha}{\partial t} \tag{D.1}$$

$$-\vec{K} = \frac{\partial \alpha}{\partial \vec{x}}, \tag{D.2}$$

and the group speed which is defined as follows:

$$\vec{c_g} = \frac{\partial \omega}{\partial \vec{K}} = \frac{\mathrm{dx}}{\mathrm{dt}}, \tag{D.3}$$

because ray theory follows the short wave energy in rays. Recalling that the dispersion relation equation 2.19 is of the form $\omega = \omega(k,l,m,x,y,z,t)$ and using expressions D.1 and D.2 to write ω in a different form yields the following equation:

$$\omega = \frac{\partial \alpha}{\partial t} = \omega\left(-\frac{\partial \alpha}{\partial x}, -\frac{\partial \alpha}{\partial y}, -\frac{\partial \alpha}{\partial z}, x, y, z, t\right), \tag{D.4}$$

The derivative with respect to $\vec{x}$ of equation D.4 is taken which becomes:

$$\frac{\partial^2 \alpha}{\partial \vec{x} \partial t} = \frac{\partial \omega}{\partial \vec{K}}\left(-\frac{\partial^2 \alpha}{\partial \vec{x} \partial \vec{x}}\right) + \frac{\partial \omega}{\partial \vec{x}}. \tag{D.5}$$

Using equations D.2 and D.3 to rewrite equation D.5 yields:

$$\frac{\partial \vec{K}}{\partial t} + \vec{c_g}\left(\frac{\partial \vec{K}}{\partial \vec{x}}\right) = -\frac{\partial \omega}{\partial \vec{x}}. \tag{D.6}$$

Assuming a frame of reference in which the wavepacket is continually tracked while moving at its group velocity, the position $\vec{x}$ changes with respect to a stationary observer according to $D\vec{x}/Dt = \vec{c}_g$ as seen by ray equation 2.33. In contrast, the changes with respect to an observer moving with the wavepacket will have the form of the material derivative described by the two elements on the left hand side of equation D.6. This yields the other ray equation (equation 2.32)